Supporting Information (SI)

A Coordination Driven 'heat-set' Zr-Gel: Efficient Fluorophore Probe for Selective Detection of Fe^{3+}, Nitrofuran based Antibiotics and Smart Approach towards UV Protection

Sumit Mondal[†], *and Debajit Sarma**[†]

[†]Department of Chemistry, Indian Institute of Technology Patna, Bihar 801106, India

*E-mail: debajit@iitp.ac.in

Contents

Methods:

Time-resolved PL measurements:

Fitting either a single-exponential or a bi-exponential function to the ensuing lifetime decays is demonstrated by equation S1, where the reduced χ2 is used to determine the virtue of the fitting.

$$\boldsymbol{I_t = A + \Sigma_{i=1}^{n} B_i exp^{-\left(\frac{t}{\tau i}\right)}}$$ ……. **equation S1**; where n is 1or 2

In order to determine the average lifetime, we employ the fitted parameters, which include the lifetime components τ_i's and their respective relative contributions, B_i's, as shown in equation S2:

$$\boldsymbol{\tau_{avg} = \frac{\sum_{i=1}^{n} B_i \tau_i^2}{\sum_{i=1}^{n} B_i \tau_i}}$$ ……. **equation S2**; where n is 1or 2 **(Table S3).**

Characterization:

The Powder X-Ray Diffraction (PXRD) pattern was recorded using a PANalytical X'Pert Pro Diffractometer that ran at 45 mA and 40 kV with Cu K radiation. The ^{1}H and ^{13}C NMR spectra were performed using a Bruker Avance II 400 spectrometer. Using an SDT Q600 (TA Instruments) and a N_2 gas flow rate of 100 mL/min, a thermogravimetric analysis (TGA) of the xerogel was carried out. The temperature was raised from room temperature to 800 °C at a rate of 10 °C min^{-1}. The surface morphology of the xerogel was examined using a Field Emission Scanning Electron Microscope (FESEM; ZEISS GEMINISEM500 assembled with an energy-dispersive X-ray spectroscopy detector). The xerogel sample was examined using a transmission electron microscope (JEOL-JEM-F200) at a 200 kV potential. The FT-IR spectra of all the samples were recorded using an ATR sampling method on a PerkinElmer Spectrum 400 instrument. The rheological measurements were carried out using a Modular Compact Rheometer by Anton Paar (MCR 302). In order to determine the storage modulus (G') and loss modulus (G"), the metallogel was scanned on a parallel plate with a 9-millimeter diameter while being subjected to 0.1% strain. All UV-Vis spectra were performed using a Shimadzu UV2500 spectrophotometer. Utilizing two-sided transparent square-faced quartz cuvettes, solution phase data from the instrument was taken (1 cm path-length). Solid-state UV-Vis spectra were collected on a JASCO V-650 spectrometer. Utilizing a Horiba Jobin Yvon Fluoromax-4 fluorescence spectrophotometer, photoluminescence (PL) spectra were acquired. In order to conduct the dispersed phase fluorescence investigation, a 4 mL four-faced transparent quartz cuvette was used. All the solution and dispersed phase photoluminescence spectra were measured using fresh Milli-Q water. The Edinburgh Instrument (model: lifeSpec II, U.K) of fluorescence spectrophotometer was used for Time-Resolved Photoluminescence (TRPL) analysis. The data was taken using a Hamamtsu MCP PMT (3809U) detector.

NMR data of the H_3TATAB linker:

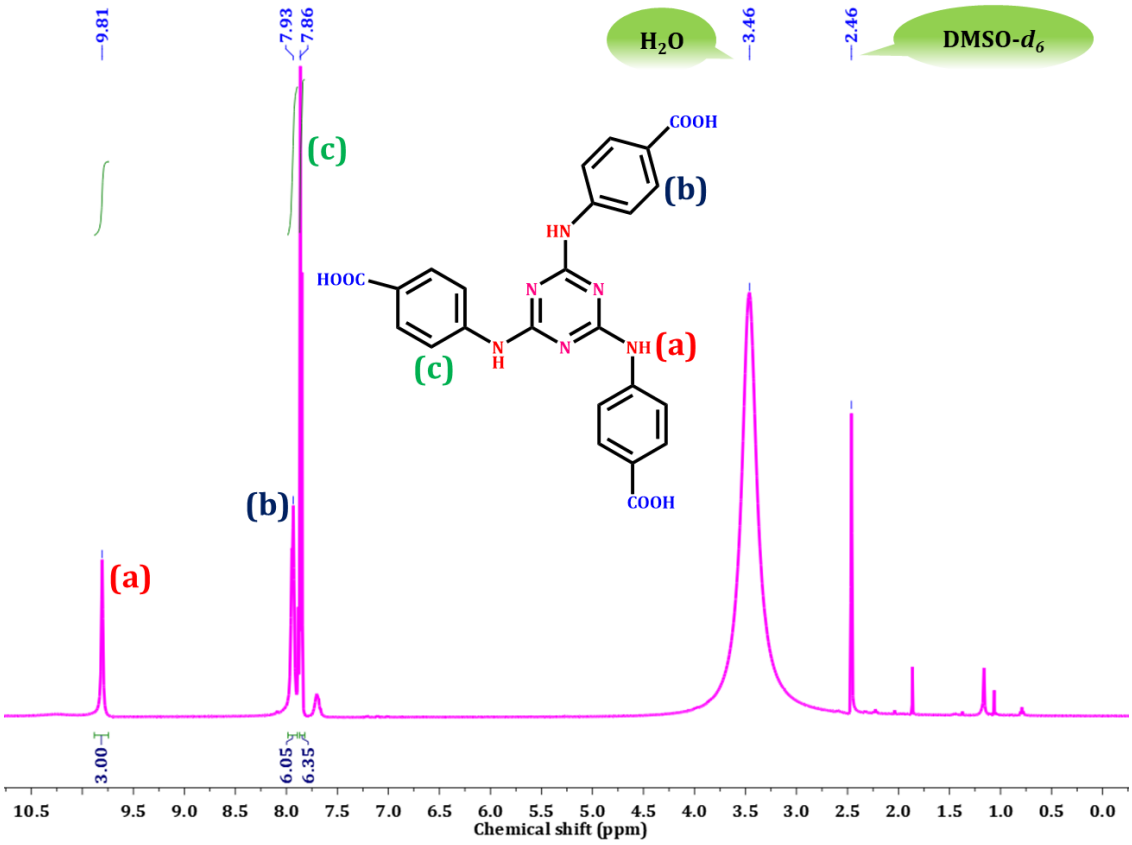

Figure S1:^{1}H-NMR spectrum of the H_3TATAB linker (400 MHz, in DMSO-d_6).

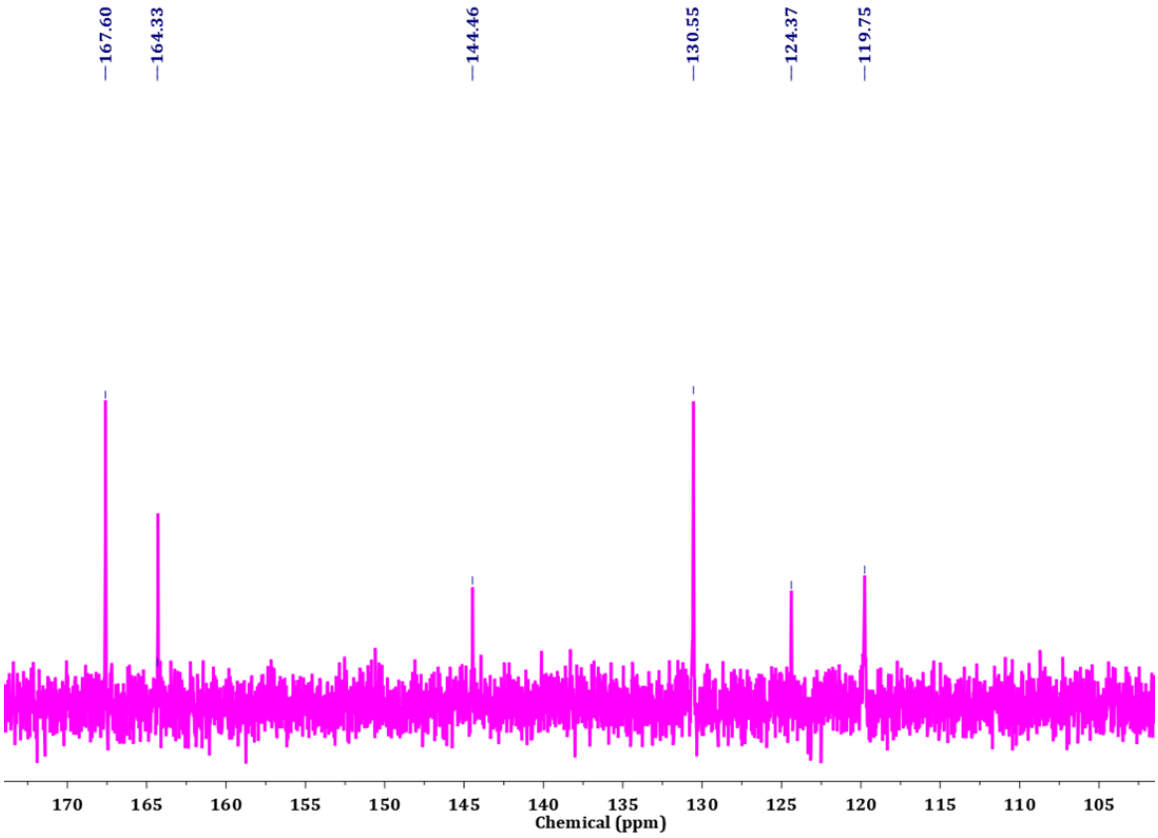

Figure S2: ^{13}C-NMR spectrum of the H_3TATAB ligand (400 MHz, in DMSO-d_6).

Synthesis, characterization of the metallogel and xerogel:
Table S1: Gelation study in various solvent combinations

Sl. No.	Solvent used	Gelation ability	Temperature	Image
1.	DMF/Water	Gel formation happen	90 °C	
2.	DMF/MeOH	White precipitate	90 °C	
3.	DMF/EtOH	Little turbidity	90 °C	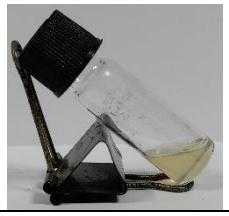
4.	DMSO/Water	Weak gelation	90 °C	
5.	DMSO/ MeOH	White precipitate	90 °C	
6.	DMSO/ EtOH	Clear solution	90 °C	

7.	THF	Linker is not soluble	-	
8.	Hexane	Linker is not soluble	-	
9.	Chloroform	Linker is not soluble	-	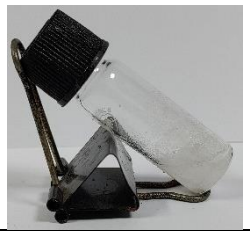

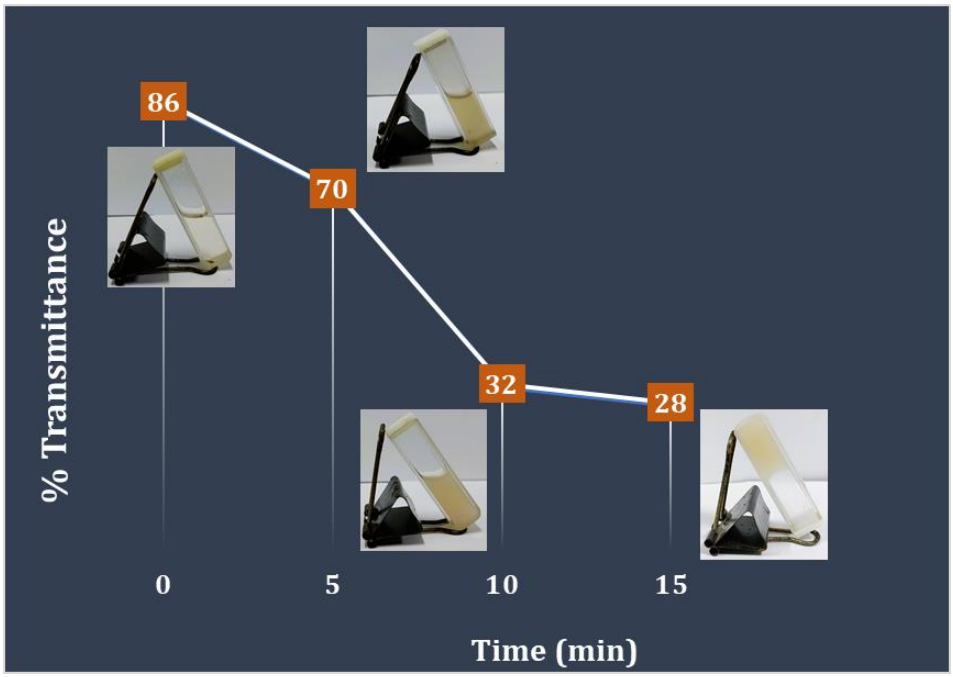

Figure S3: Turbidity measurments which correlates with naked eye test and transmittance (100 T% at 500 nm wavelength) at different time interval of the gelation process.

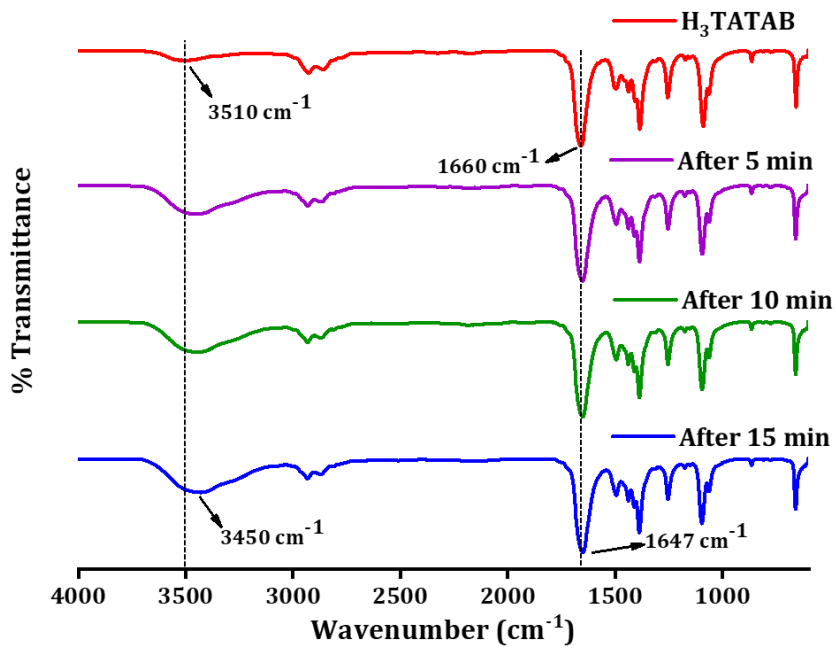

Figure S4: FT-IR analysis of the linker and different time interval gelation process.

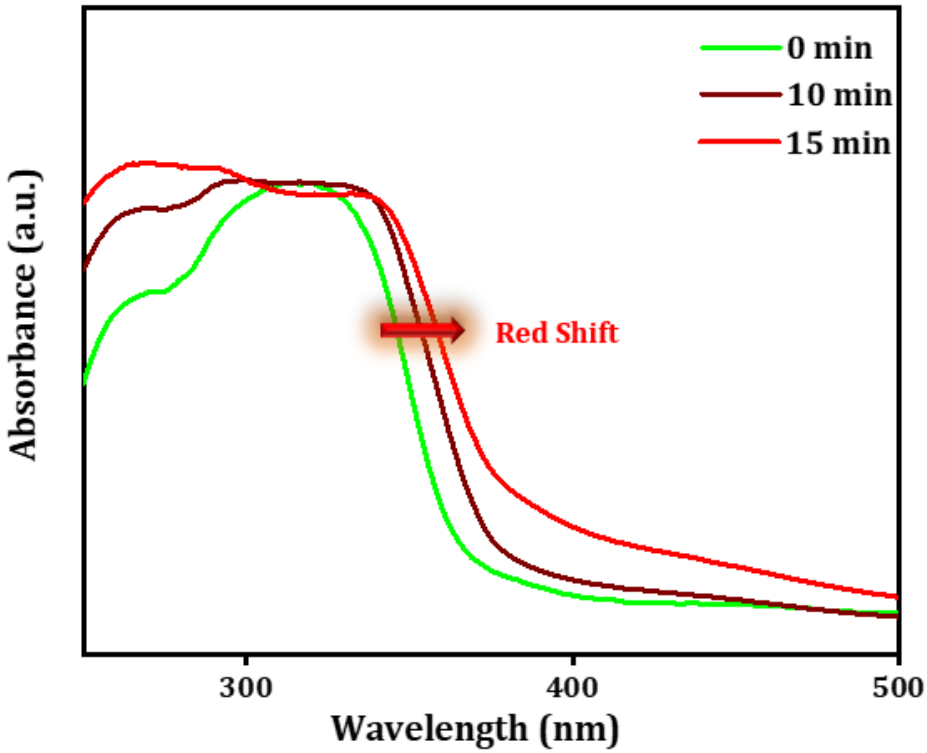

Figure S5: DRS spectra analysis of reaction mixtures (in different time interval for sol to gel transition).

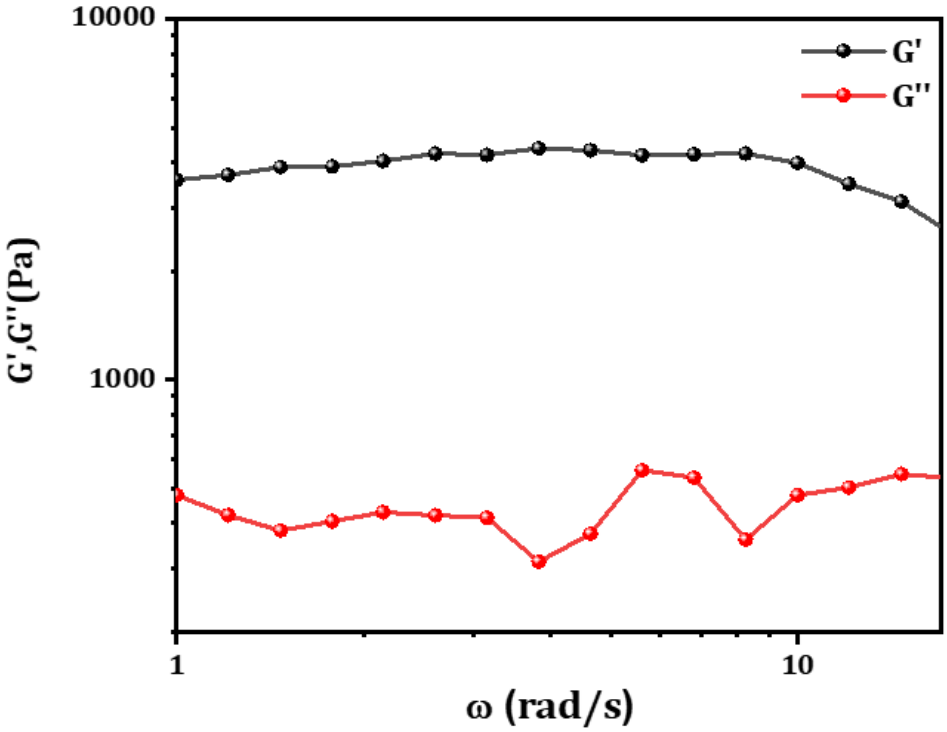

Figure S6: Dynamic angular frequency sweep vs. gain modulus (G′) and loss modulus (G″) of the Zr-CPG.

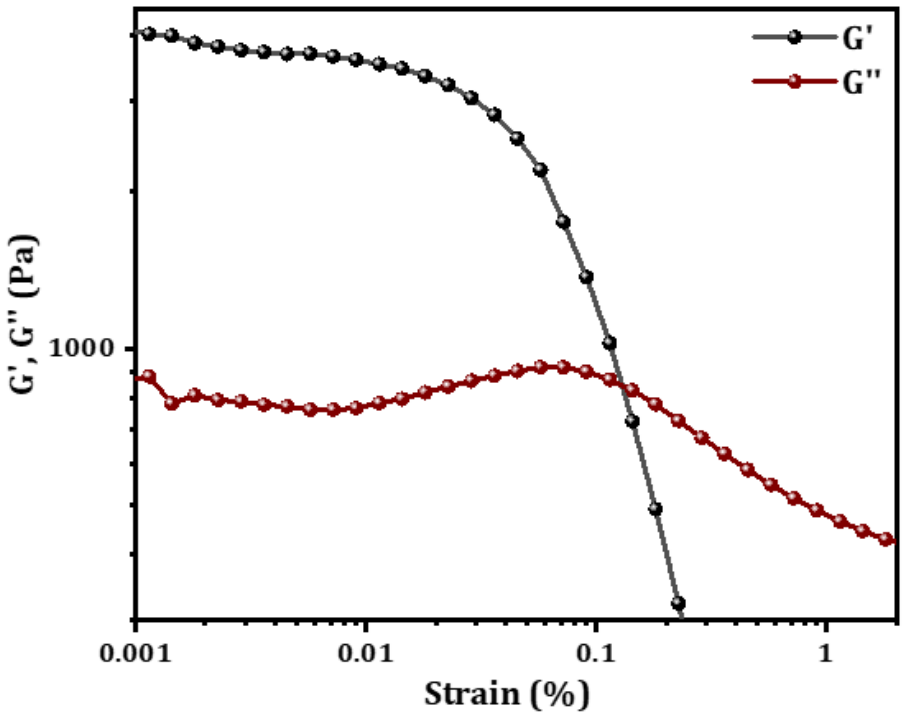

Figure S7: Dynamic Strain sweep vs. gain modulus (G′) and loss modulus (G″) of the Zr-CPG.

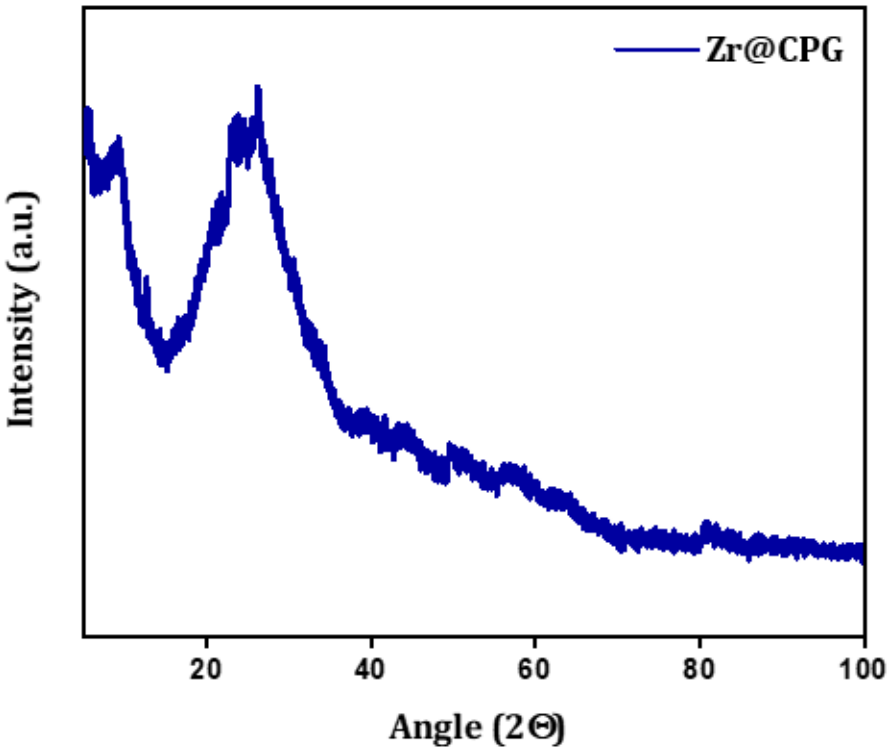

Figure S8: PXRD pattern of Zr-CPG xerogel.

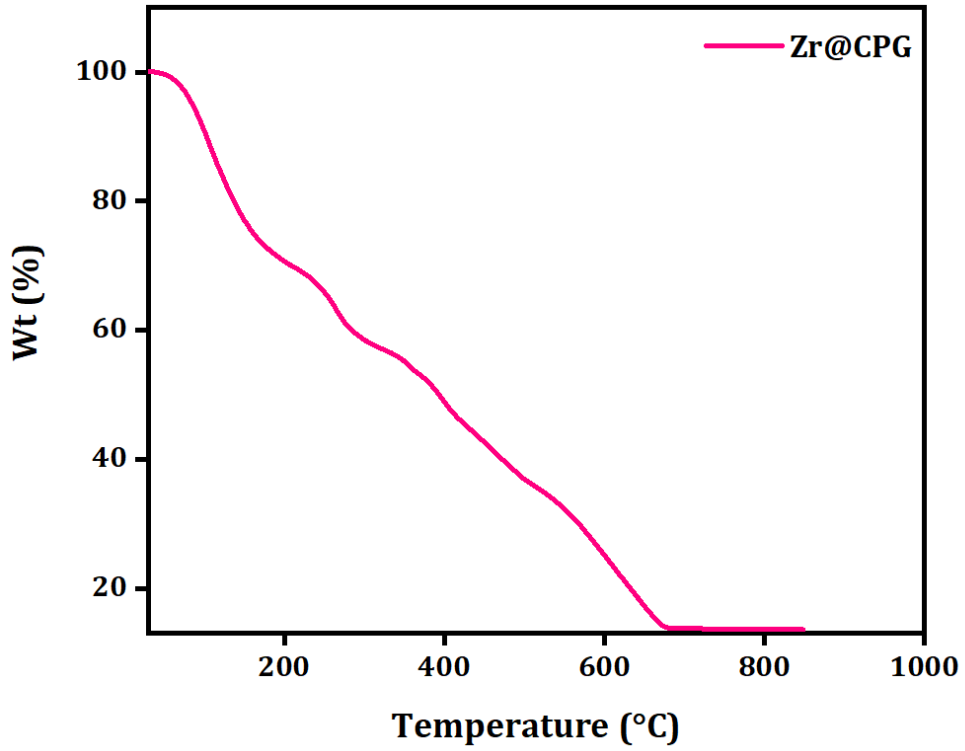

Figure S9: TGA analysis of Zr-CPG xerogel.

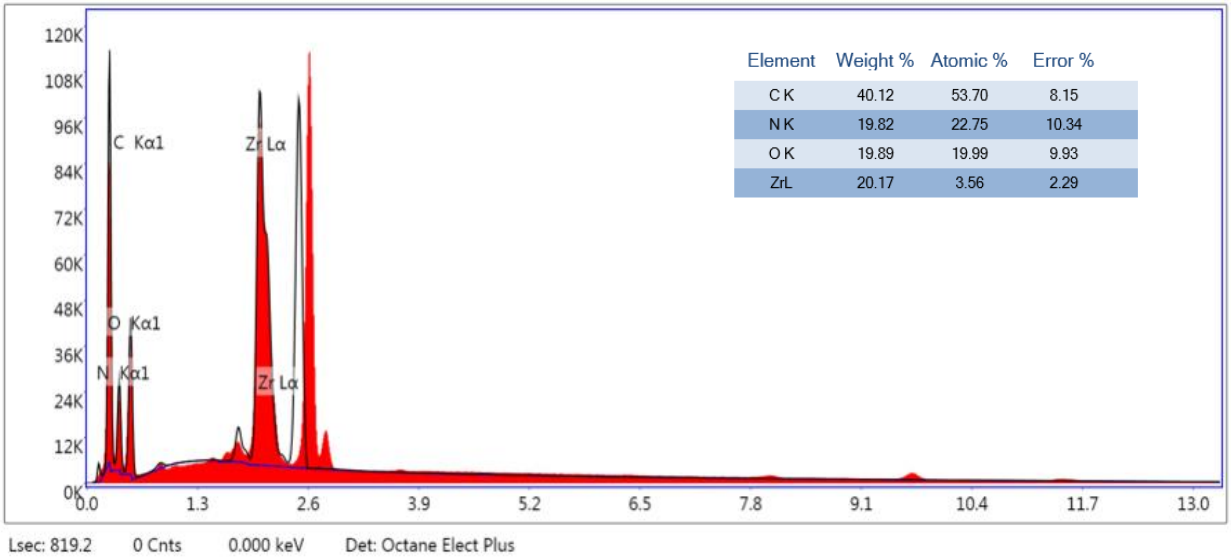

Element	Weight %	Atomic %	Error %
C K	40.12	53.70	8.15
N K	19.82	22.75	10.34
O K	19.89	19.99	9.93
ZrL	20.17	3.56	2.29

Figure S10: EDS analysis of the Zr-CPG xerogel with elemental dot mapping image.

Photophysical properties of the Zr-CPG xerogel:

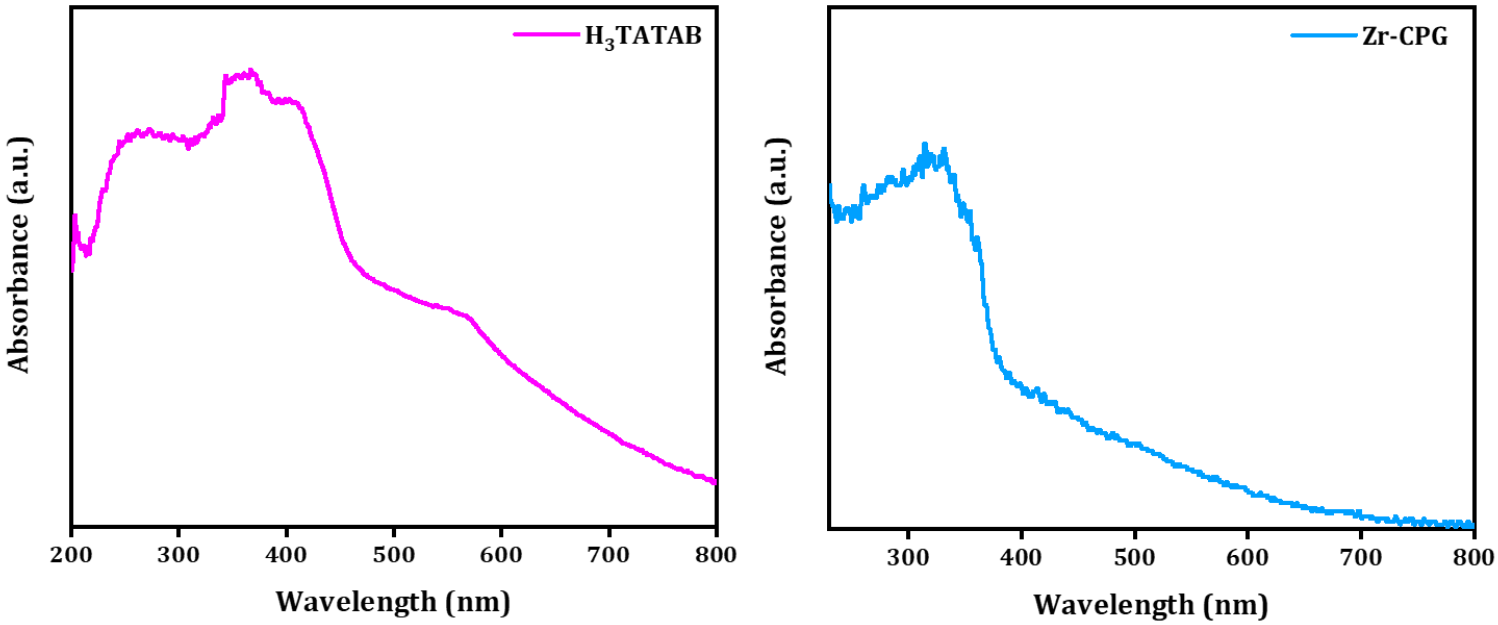

Figure S11: Solid state UV -Vis spectra of (a) linker (H_3TATAB) and (b) Zr-CPG xerogel.

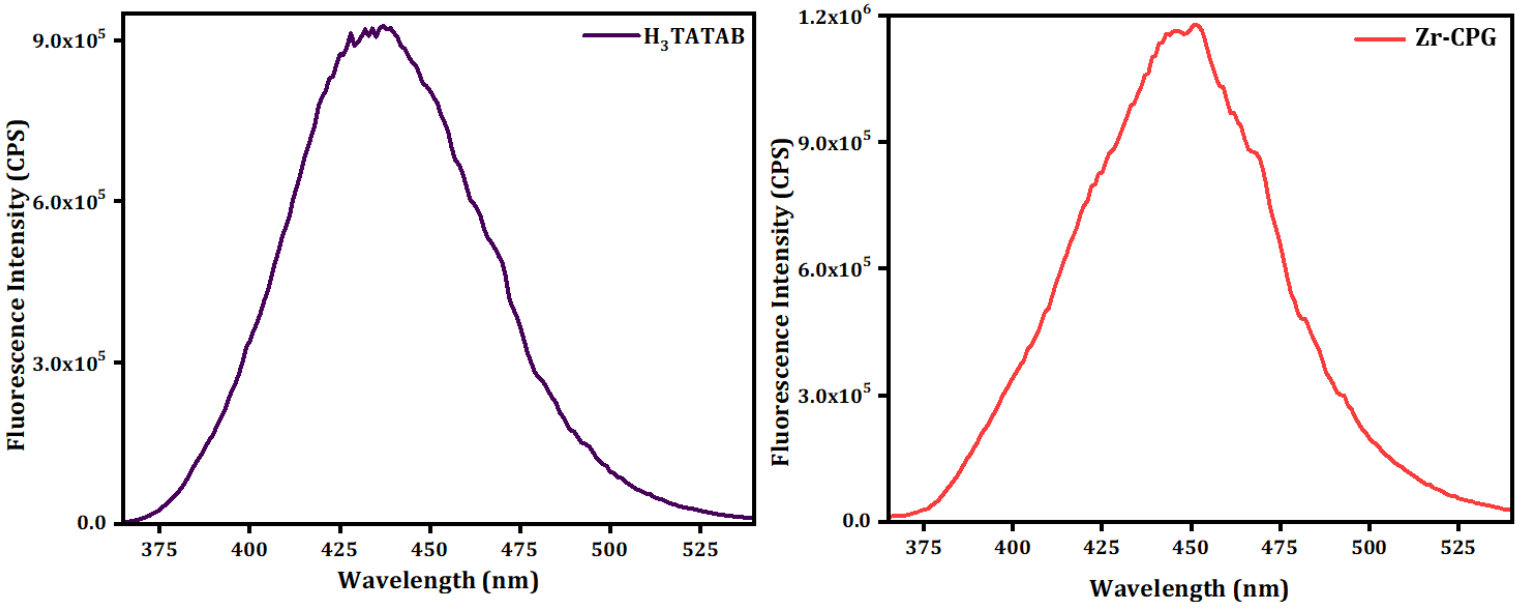

Figure S12: Solid state photoluminescence spectra of (a) linker (H_3TATAB) and (b) Zr-CPG xerogel.

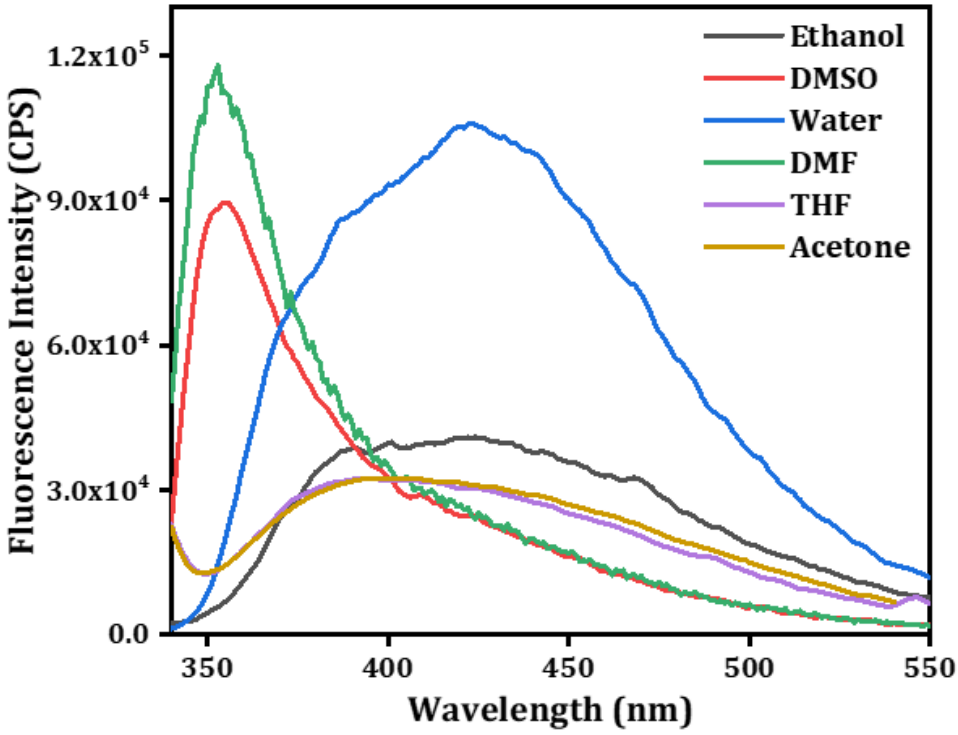

Figure S13: Solvent dependent photoluminescence study of the Zr-CPG xerogel.

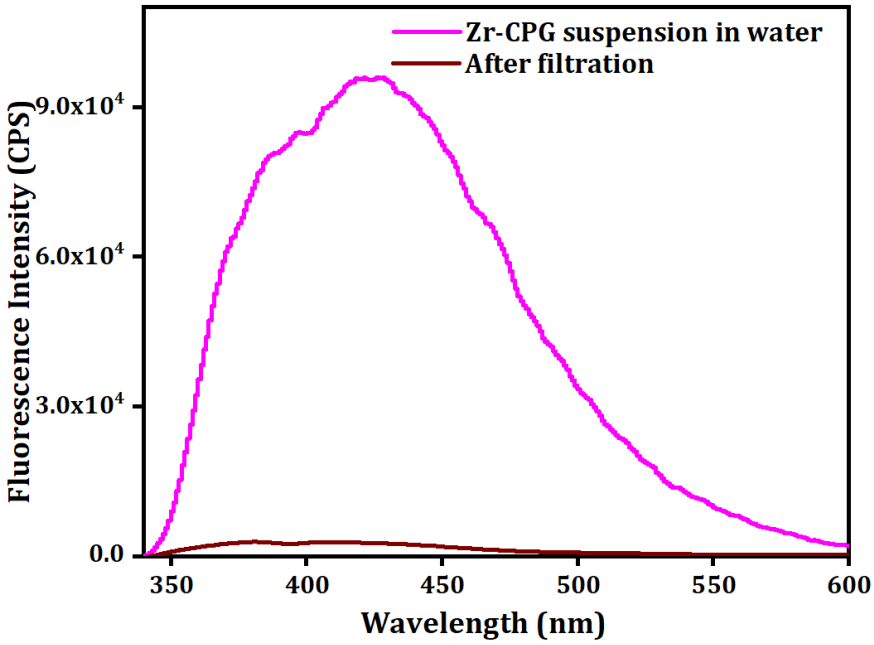

Figure S14: Leaching test for Zr-CPG xerogel suspension in water.

Quenching behaviour of Zr-CPG's luminescent peak upon addition of different metal ions (Figure S15a-S15l):

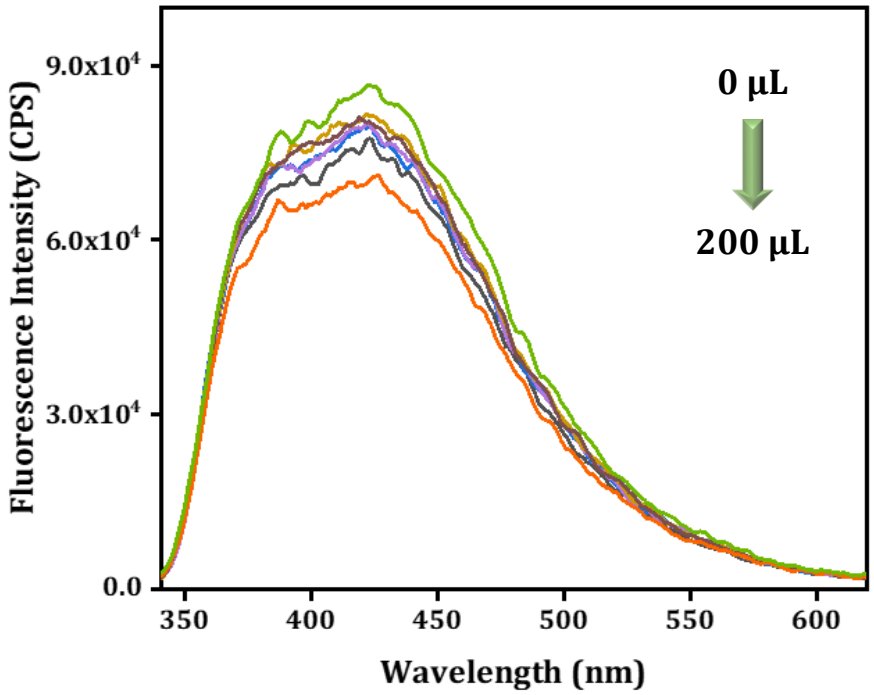

Figure 15a: Quenching of the luminescent peak of Zr-CPG xerogel upon addition of Fe^{2+}(10 mM, up to 200 µL).

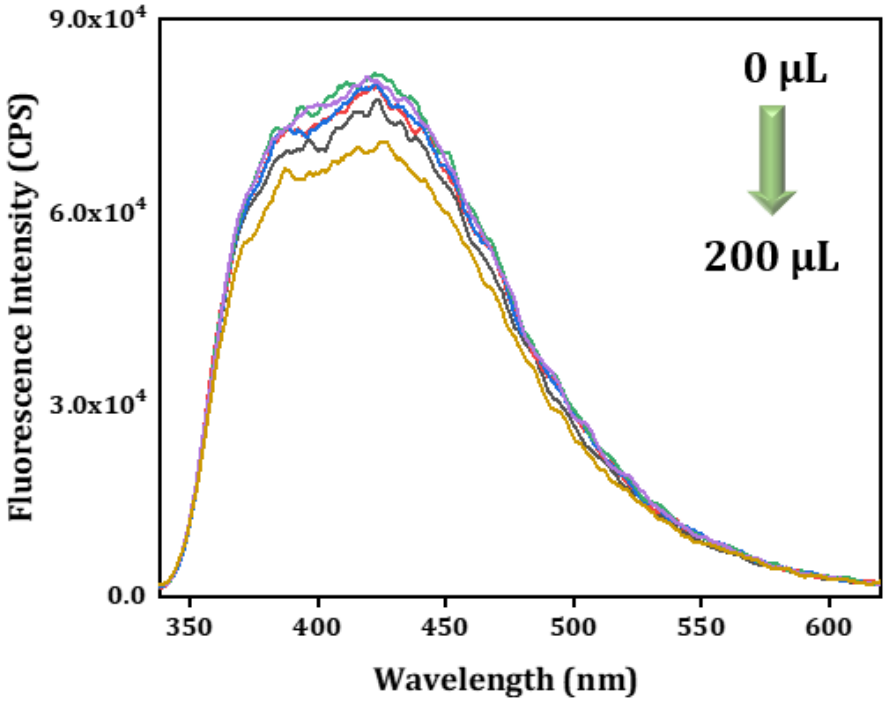

Figure S15b: Quenching of the luminescent peak of Zr-CPG xerogel upon addition of Zn^{2+} (10 mM, up to 200 µL).

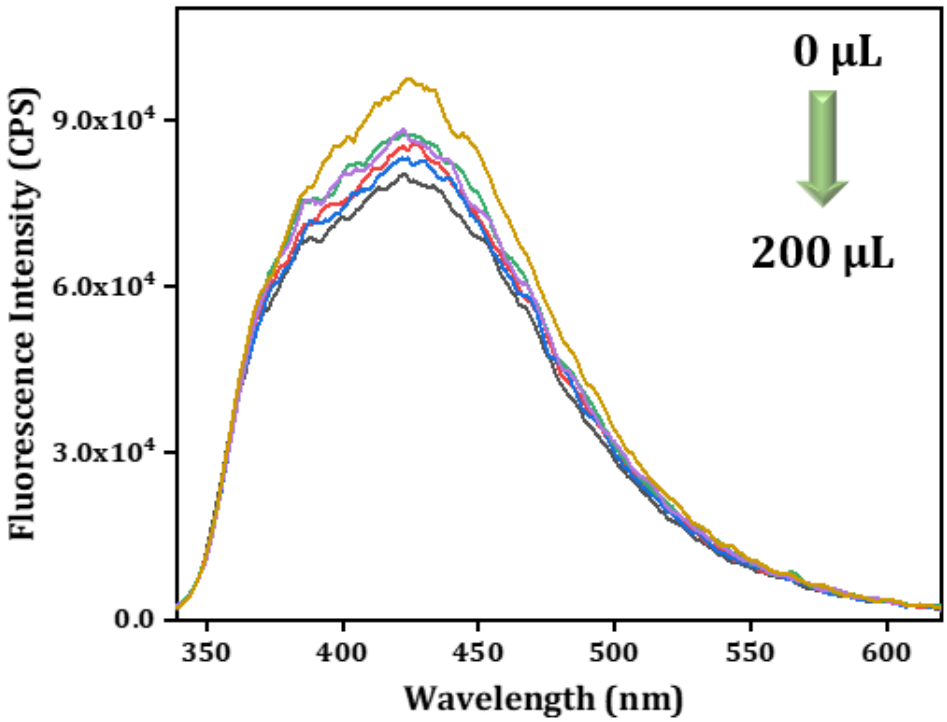

Figure S15c: Quenching of the luminescent peak of Zr-CPG xerogel upon addition of Na^{+} (10 mM, up to 200 µL).

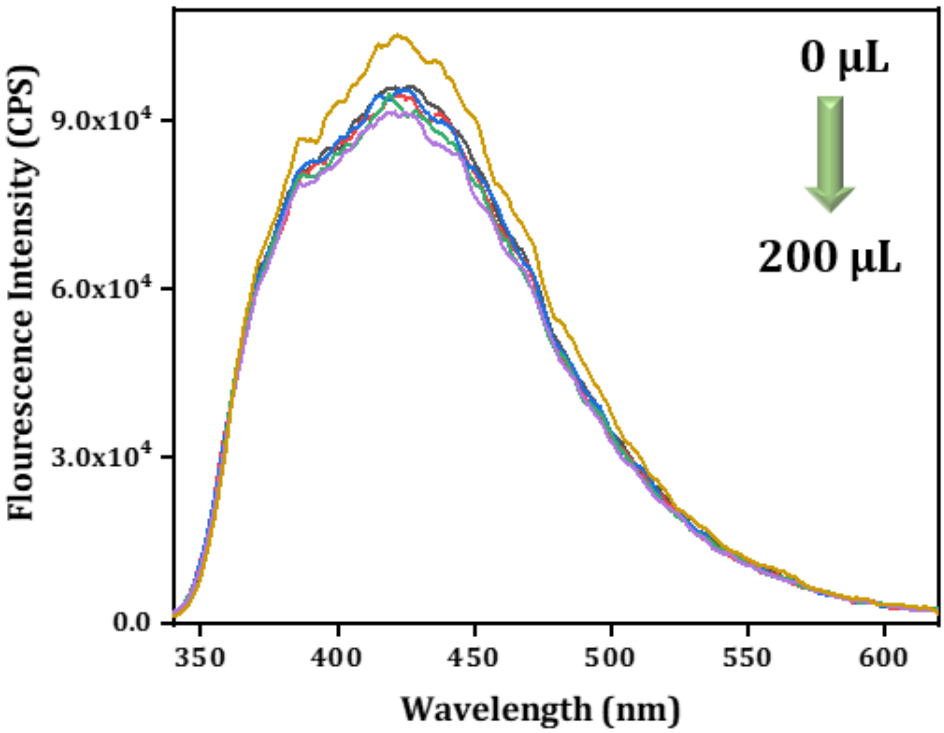

Figure S15d: Quenching of the luminescent peak of Zr-CPG xerogel upon addition of Al^{3+} (10 mM, up to 200 µL).

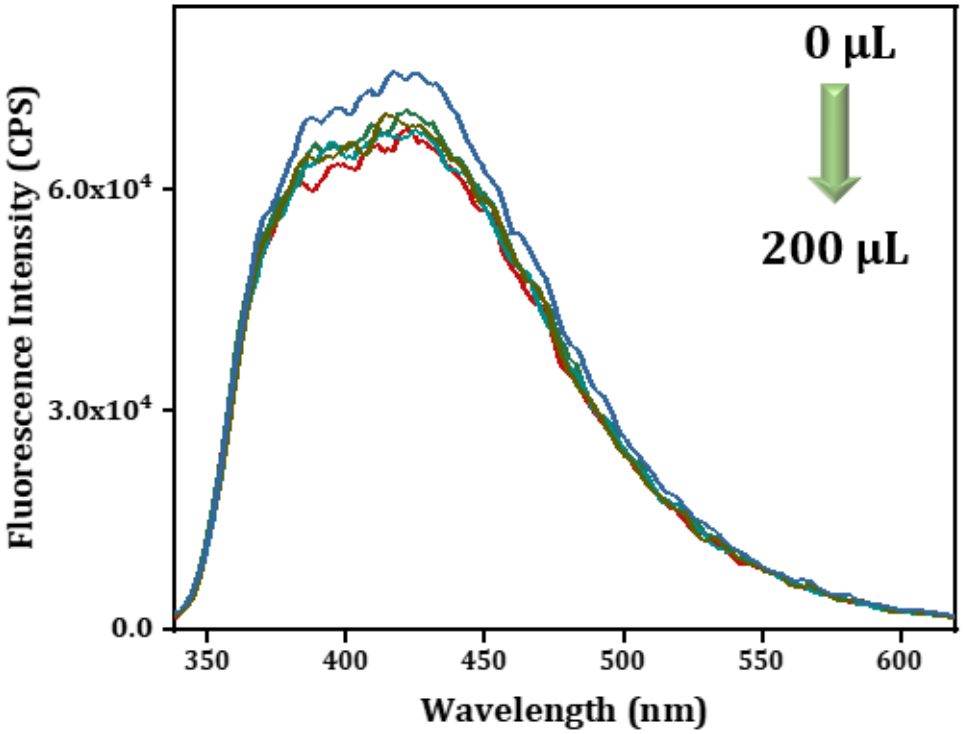

Figure S15e: Quenching of the luminescent peak of Zr-CPG xerogel upon addition of Co^{2+} (10 mM, up to 200 µL).

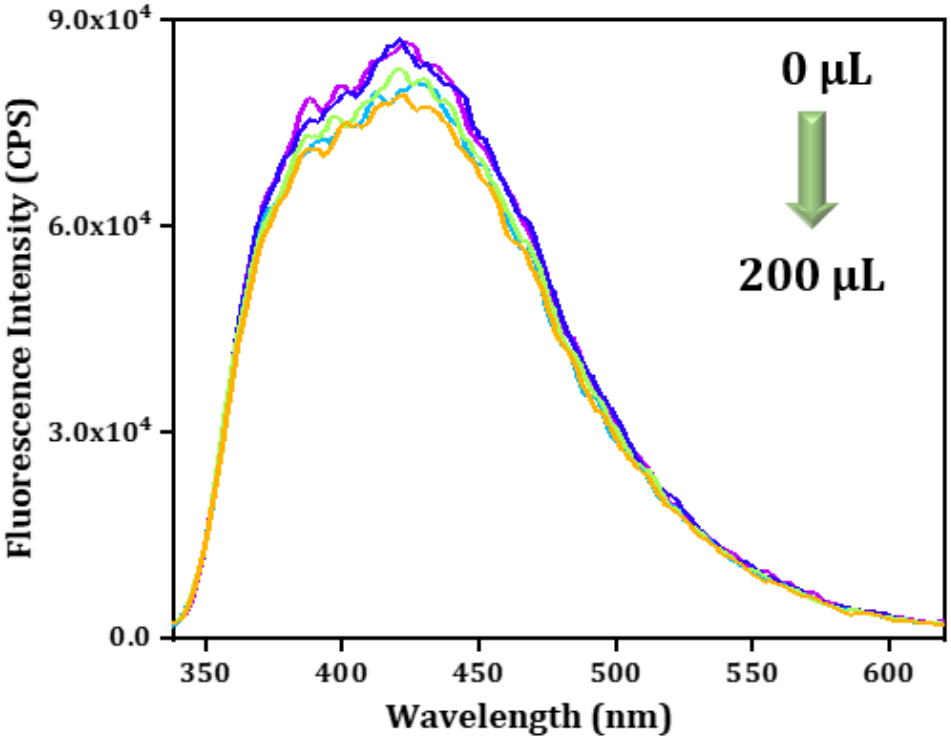

Figure S15f: Quenching of the luminescent peak of Zr-CPG xerogel upon addition of Cu^{2+} (10 mM, up to 200 µL).

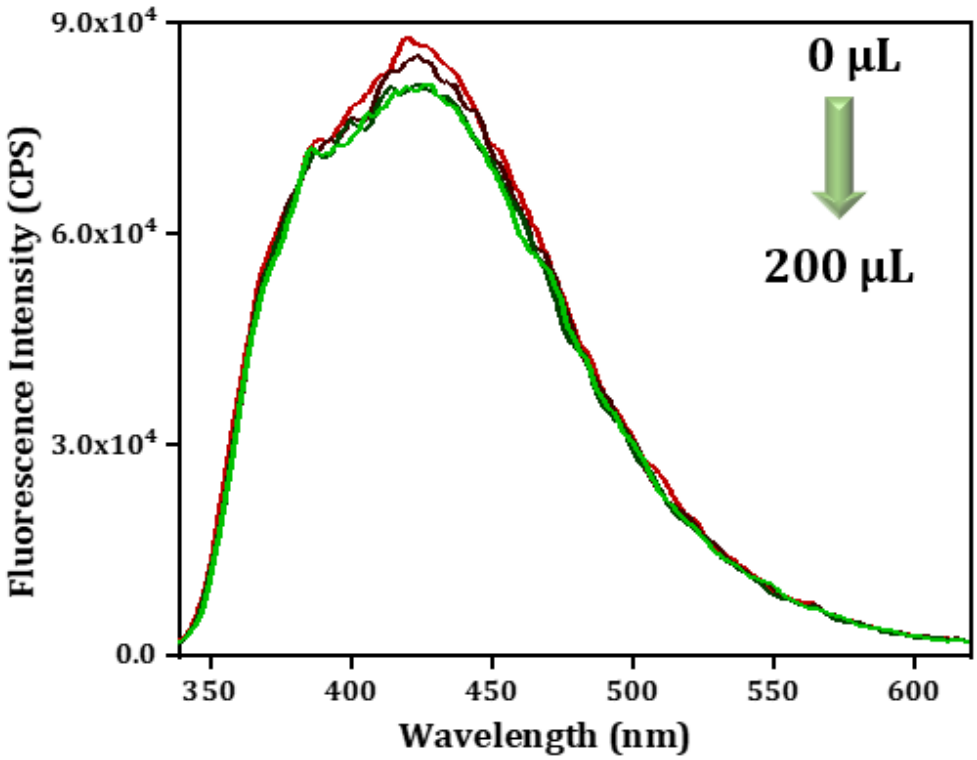

Figure S15g: Quenching of the luminescent peak of Zr-CPG xerogel upon addition of Cr^{3+} (10 mM, up to 200 µL).

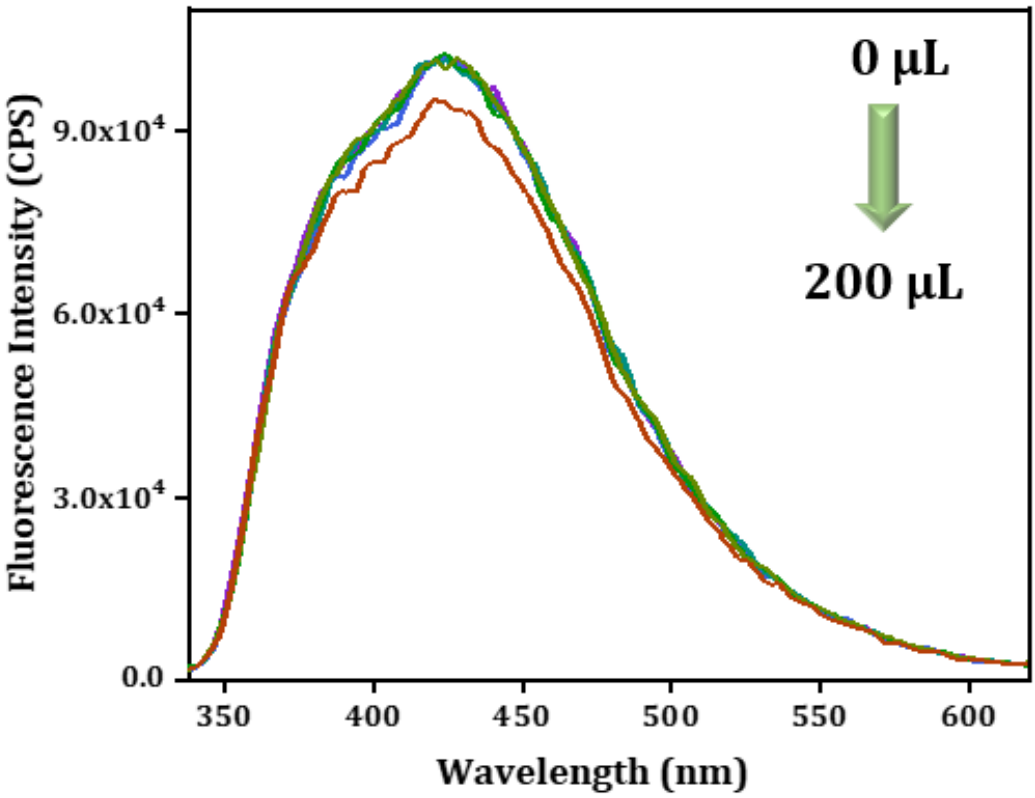

Figure S15h: Quenching of the luminescent peak of Zr-CPG xerogel upon addition of Hg^{2+} (10 mM, up to 200 µL).

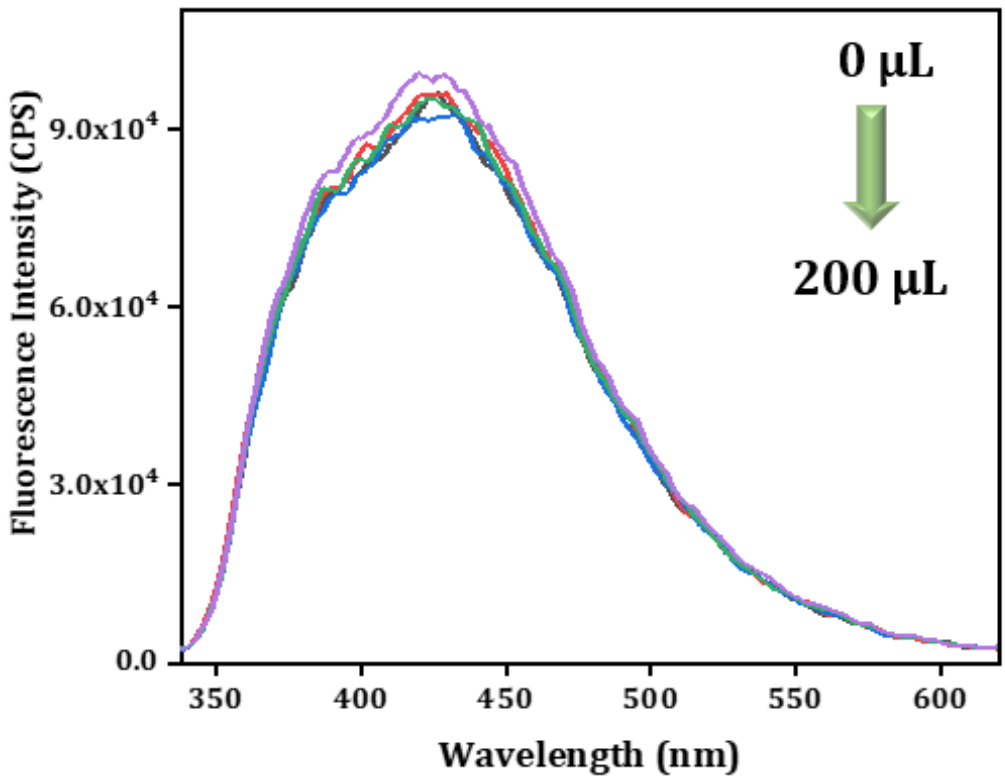

Figure S15i: Quenching of the luminescent peak of Zr-CPG xerogel upon addition of K^+ (10 mM, up to 200 µL).

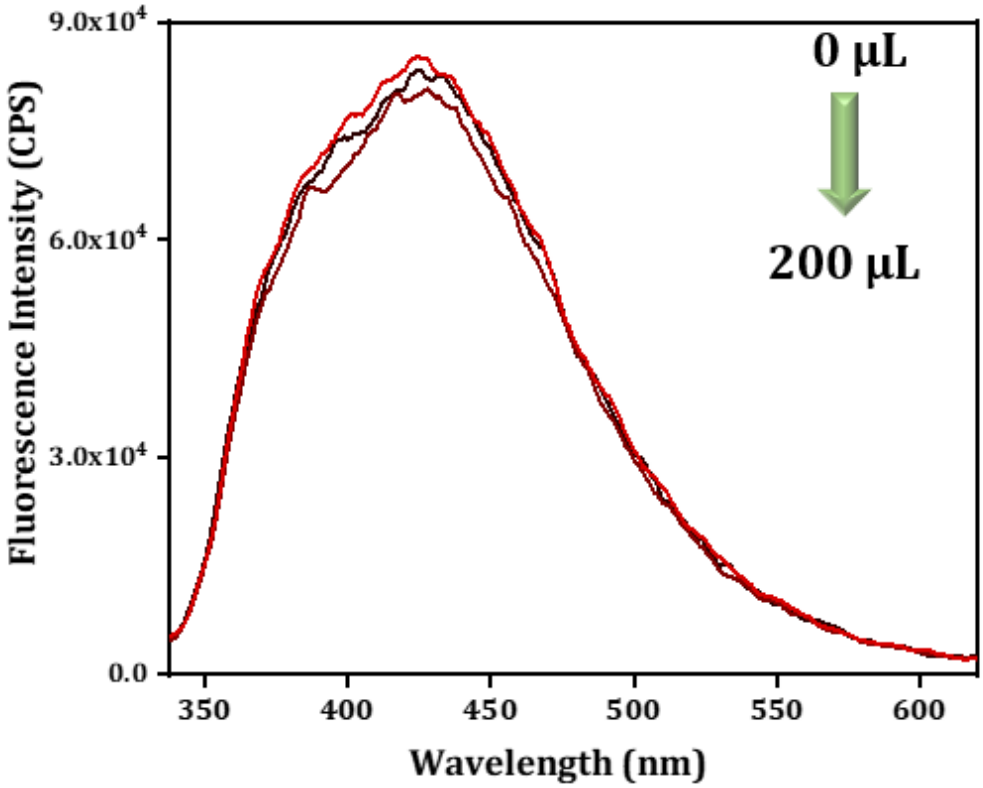

Figure S15j: Quenching of the luminescent peak of Zr-CPG xerogel upon addition of Ca^{2+} (10 mM, up to 200 µL).

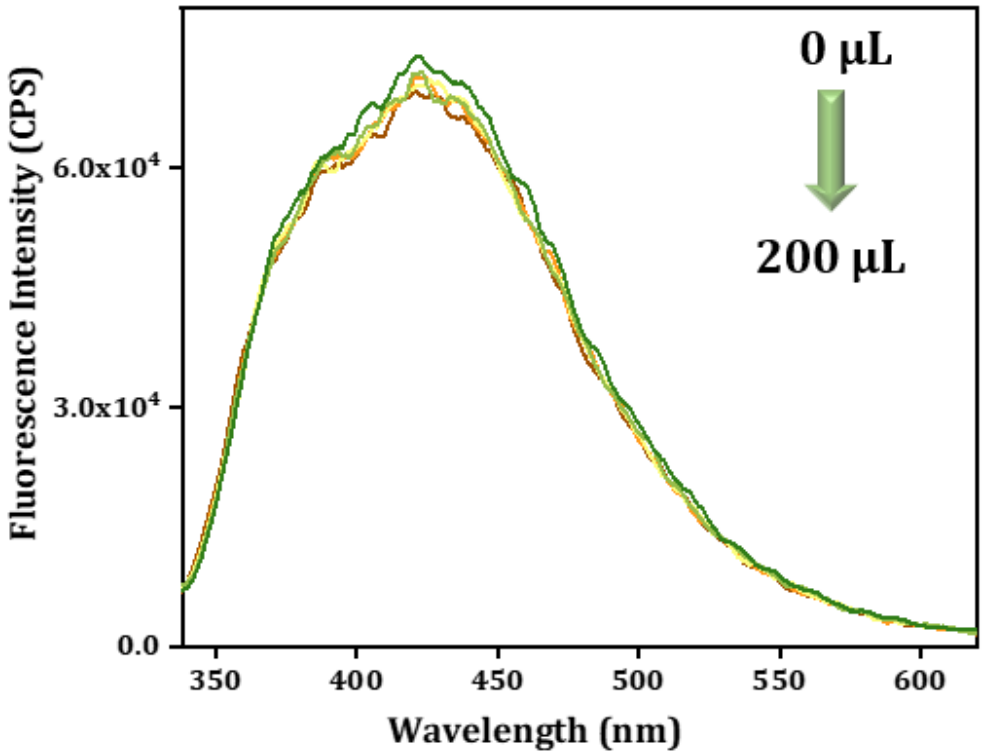

Figure S15k: Quenching of the luminescent peak of Zr-CPG xerogel upon addition of Ni^{2+} (10 mM, up to 200 µL).

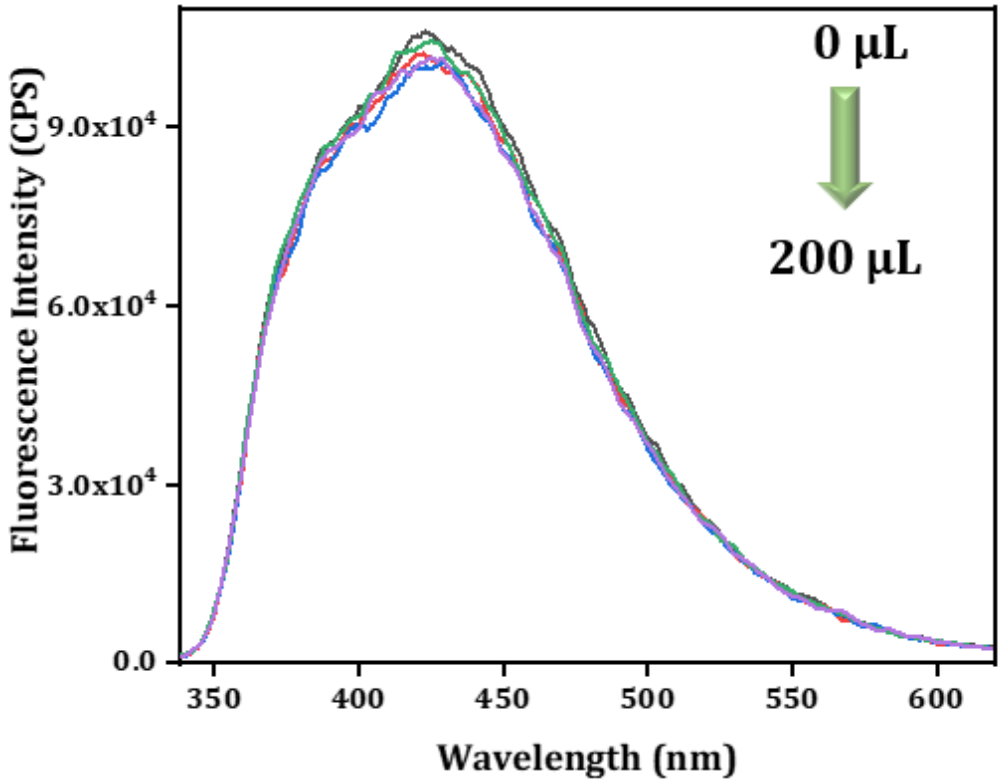

Figure S15l: Quenching of the luminescent peak of Zr-CPG xerogel upon addition of Cd^{2+} (10 mM, up to 200 µL).

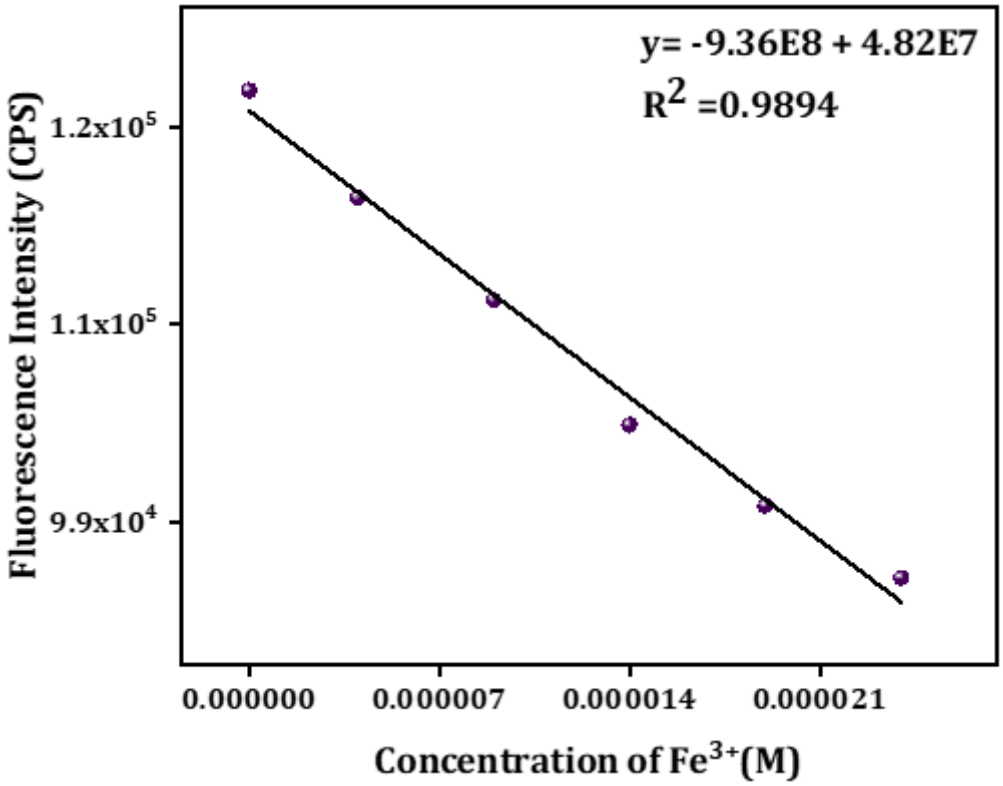

Figure S16: Fluorescence intensity changes of Zr-CPG xerogel with a function of Fe^{3+} concentration.

Fe^{3+} sensing in presence of interference metal ions (Figure S17a-S17l):

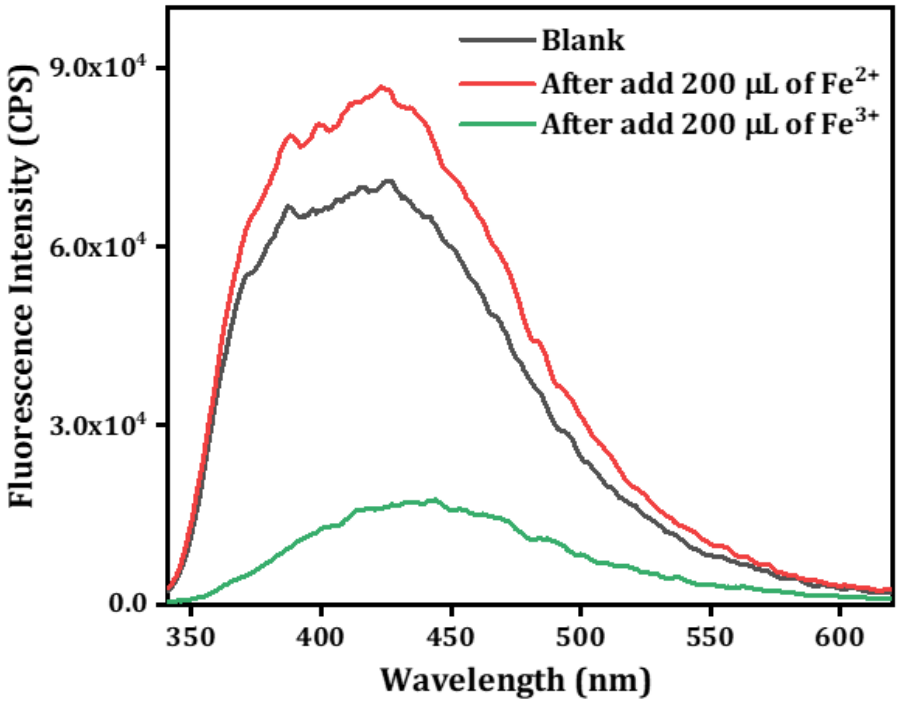

Figure 17a: Quenching behaviour of Zr-CPG xerogel characteristic peak after adding 10 mM solution of Fe^{2+} followed by Fe^{3+} in water.

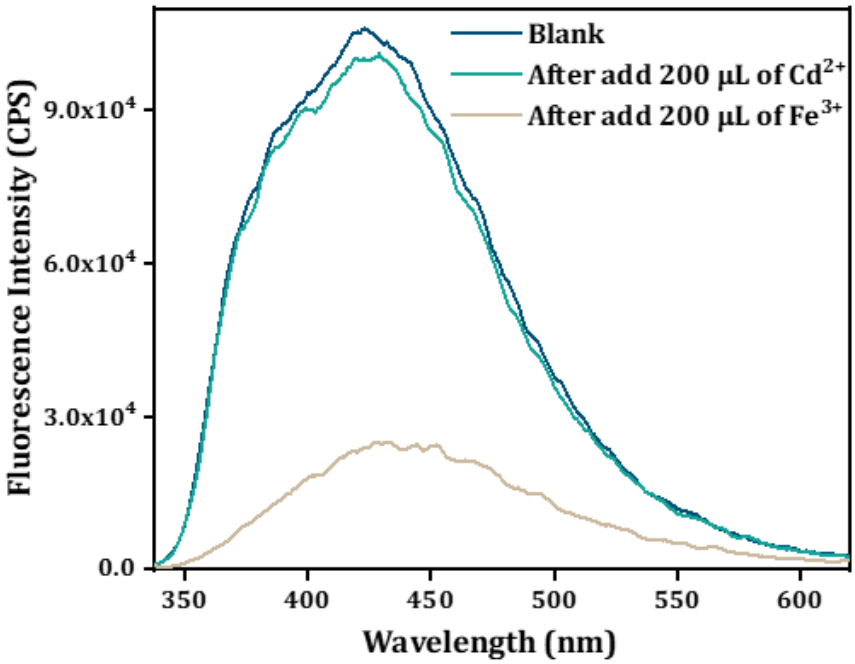

Figure S17b: Quenching behaviour of Zr-CPG xerogel characteristic peak after adding 10 mM solution of Cd^{2+} followed by Fe^{3+} in water.

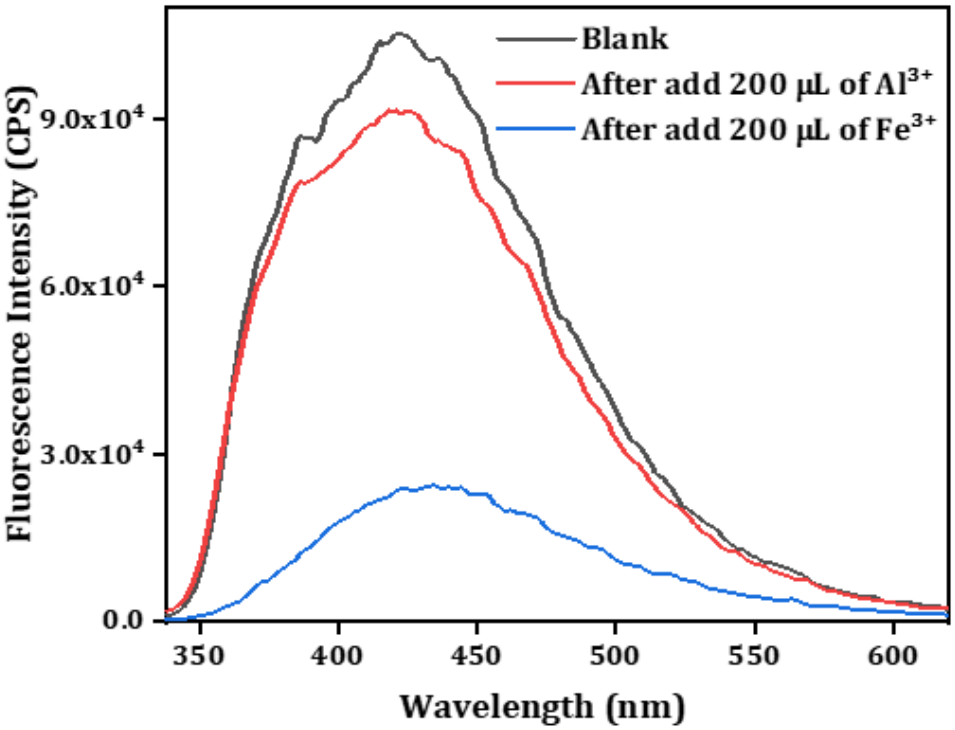

Figure S17c: Quenching behaviour of Zr-CPG xerogel characteristic peak after adding 10 mM solution of Al^{3+} followed by Fe^{3+} in water.

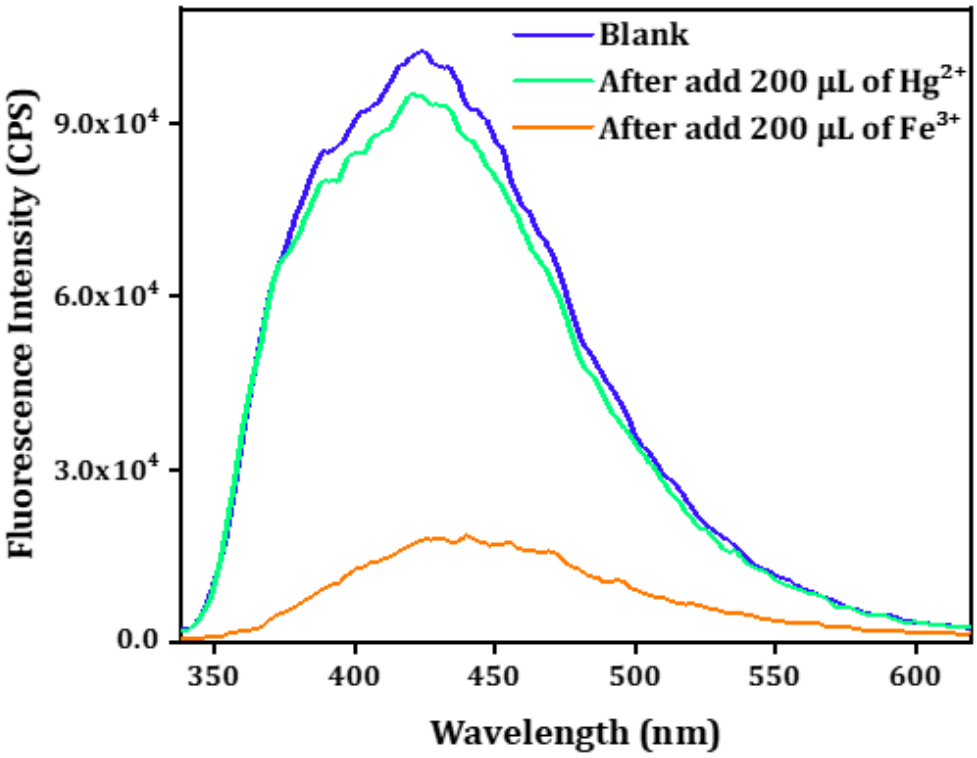

Figure S17d: Quenching behaviour of Zr-CPG xerogel characteristic peak after adding 10 mM solution of Hg^{2+} followed by Fe^{3+} in water.

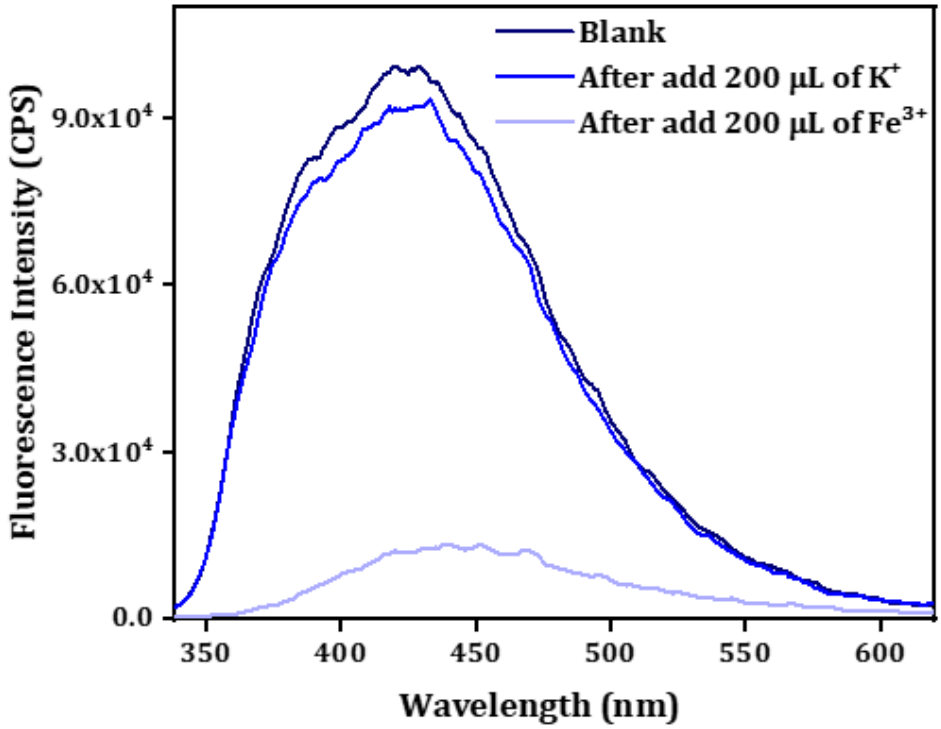

Figure S17e: Quenching behaviour of Zr-CPG xerogel characteristic peak after adding 10 mM solution of K^{+} followed by Fe^{3+} in water.

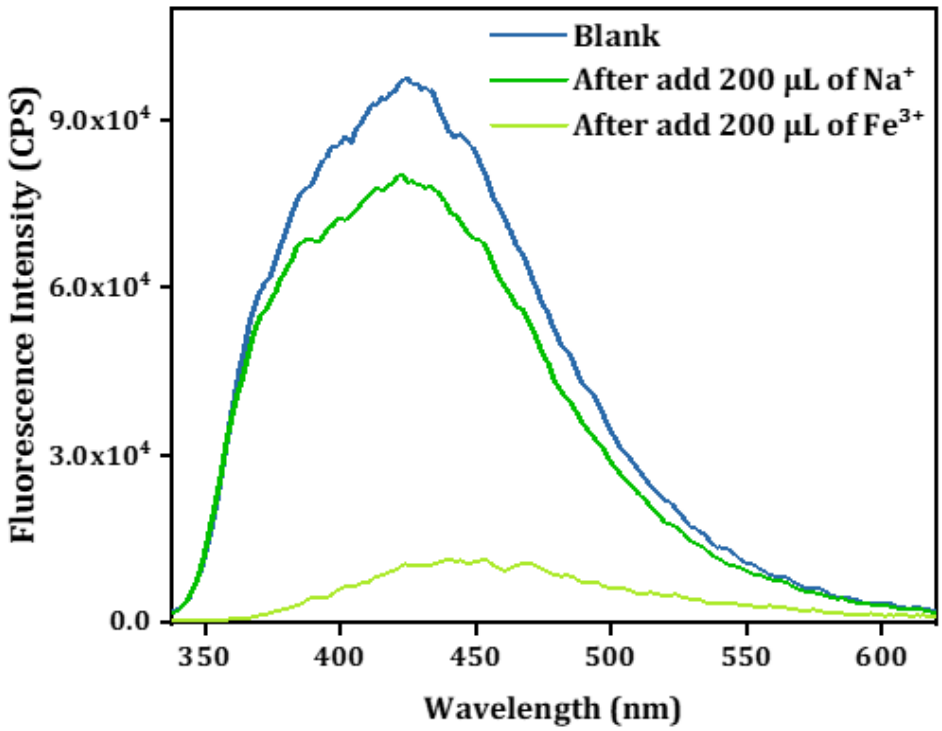

Figure S17f: Quenching behaviour of Zr-CPG xerogel characteristic peak after adding 10 mM solution of Na^{+} followed by Fe^{3+} in water.

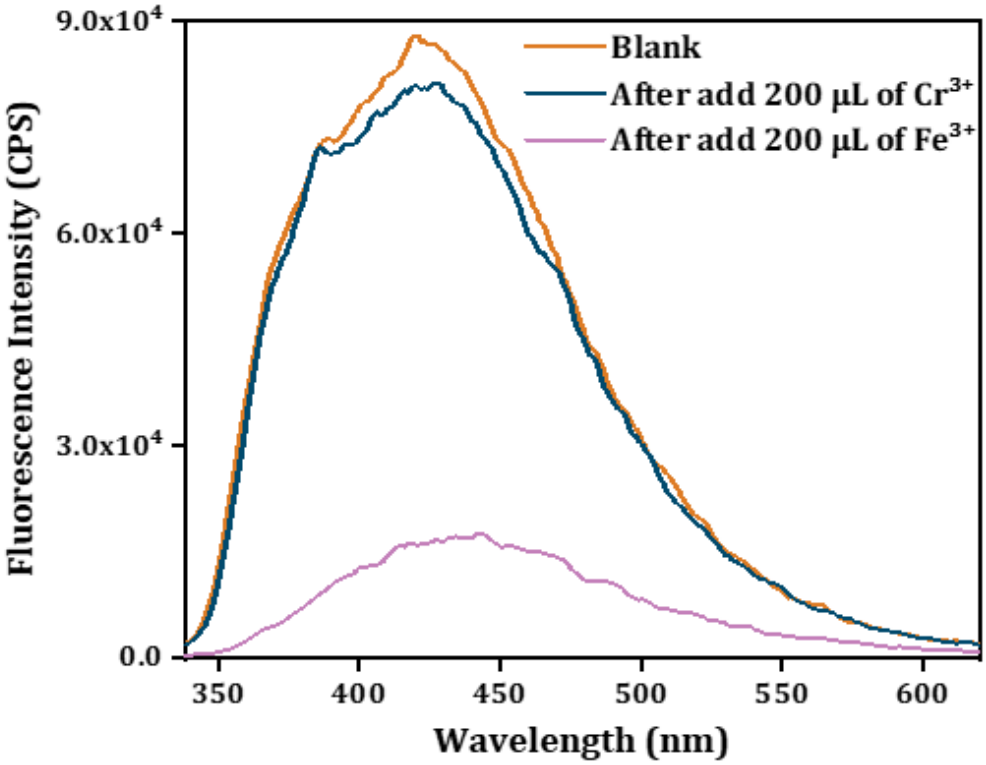

Figure S17g: Quenching behaviour of Zr-CPG xerogel characteristic peak after adding 10 mM solution of Cr^{3+} followed by Fe^{3+} in water.

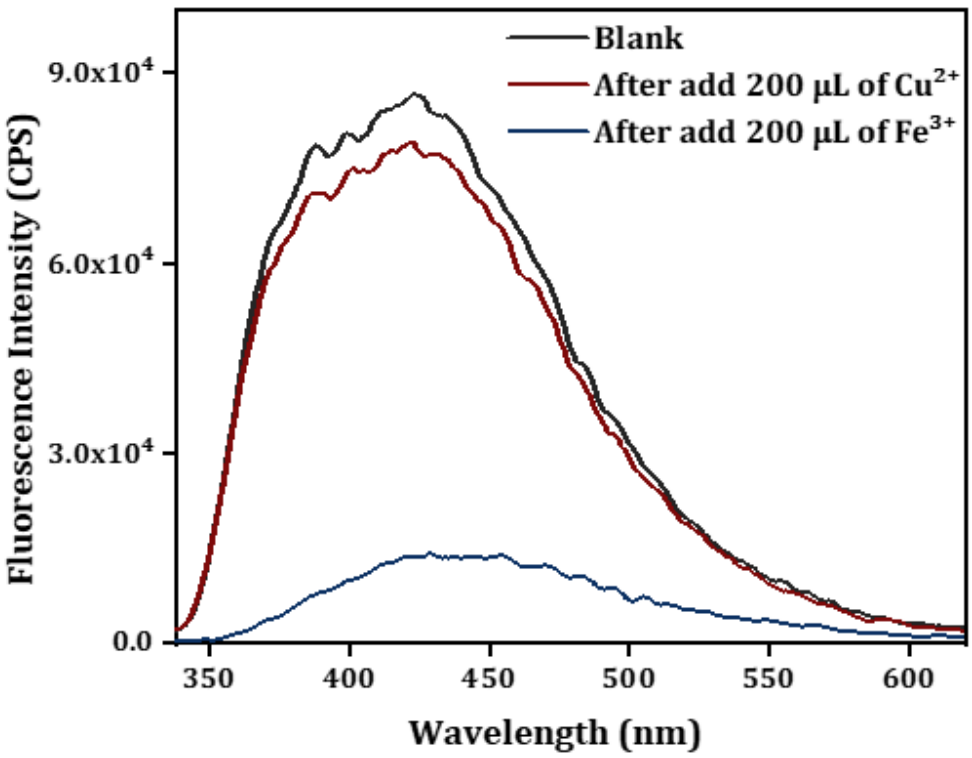

Figure S17h: Quenching behaviour of Zr-CPG xerogel characteristic peak after adding 10 mM solution of Cu^{2+} followed by Fe^{3+} in water.

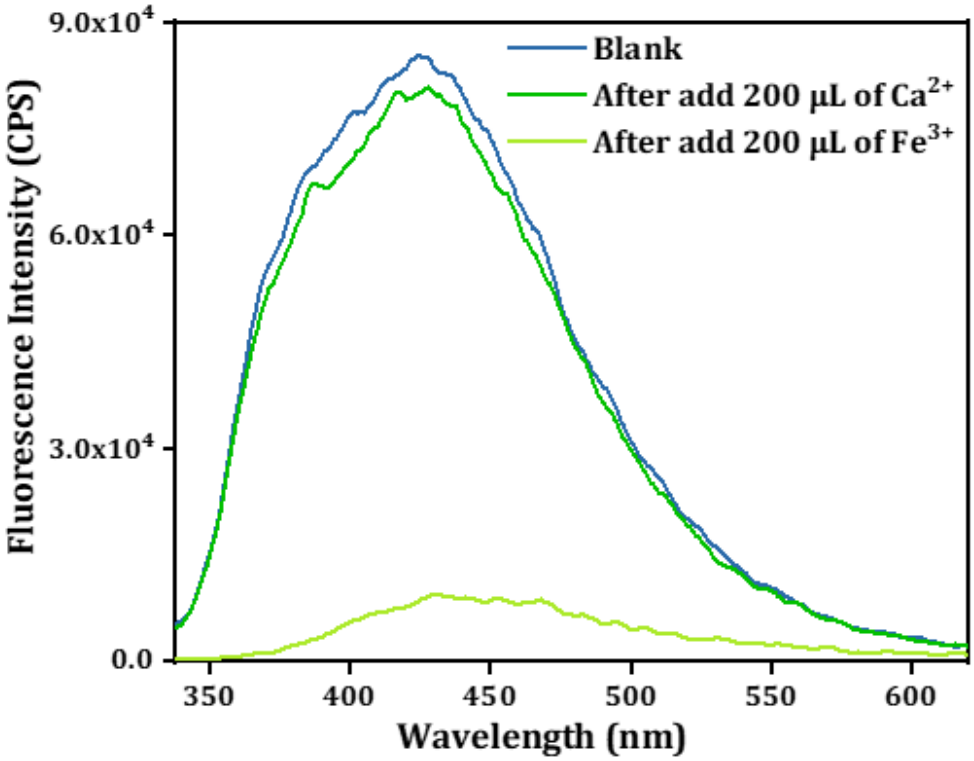

Figure S17i: Quenching behaviour of Zr-CPG xerogel characteristic peak after adding 10 mM solution of Ca^{2+} followed by Fe^{3+} in water.

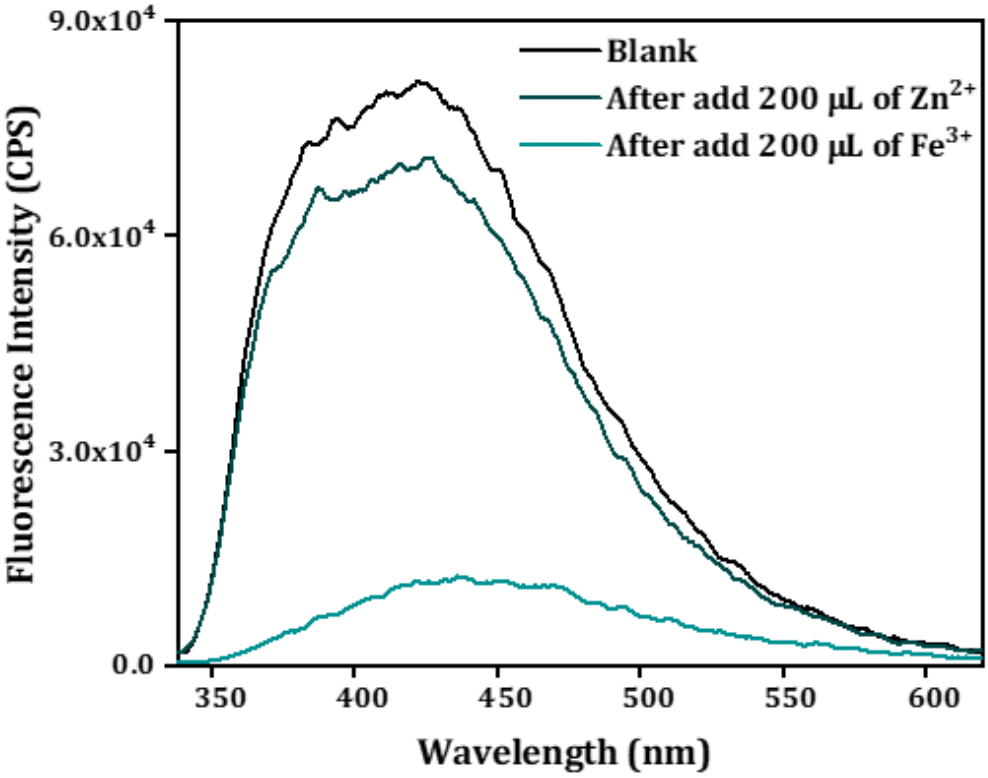

Figure S17j: Quenching behaviour of Zr-CPG xerogel characteristic peak after adding 10 mM solution of Zn^{2+} followed by Fe^{3+} in water.

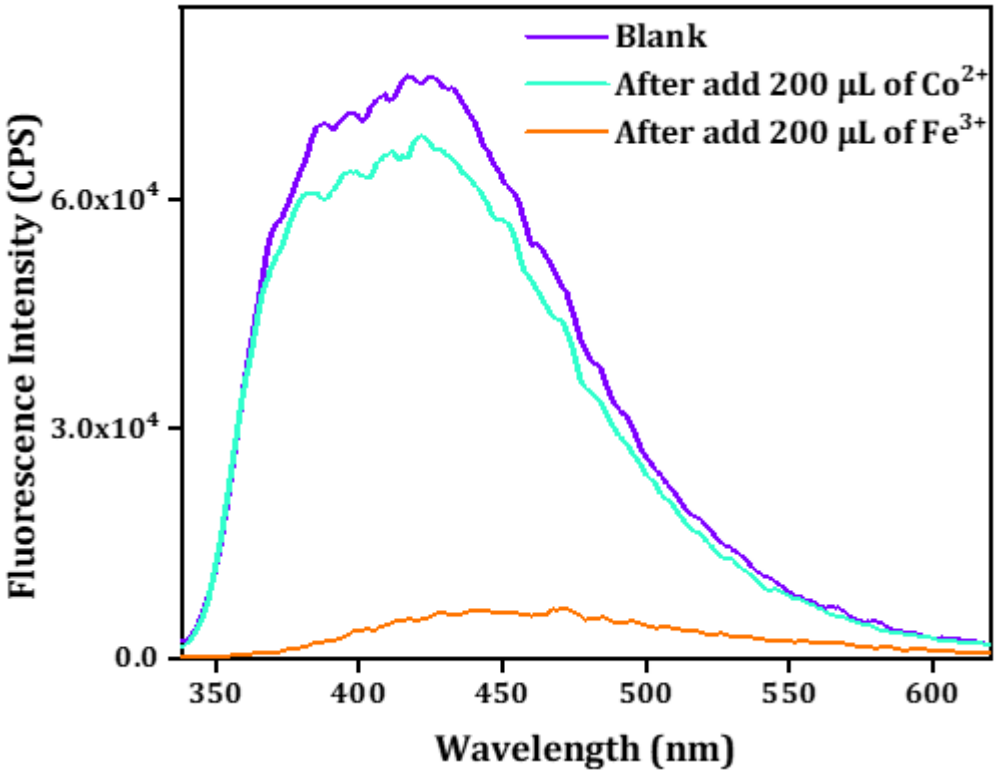

Figure S17k: Quenching behaviour of Zr-CPG xerogel characteristic peak after adding 10 mM solution of Co^{2+} followed by Fe^{3+} in water.

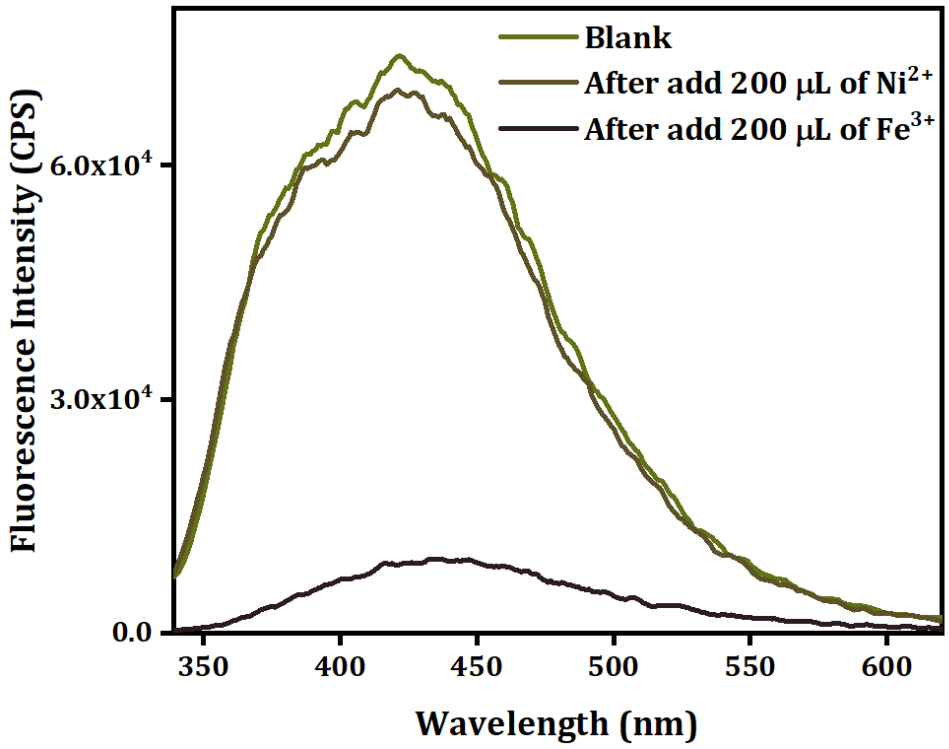

Figure S17l: Quenching behaviour of Zr-CPG xerogel characteristic peak after adding 10 mM solution of Ni^{2+} followed by Fe^{3+} in water.

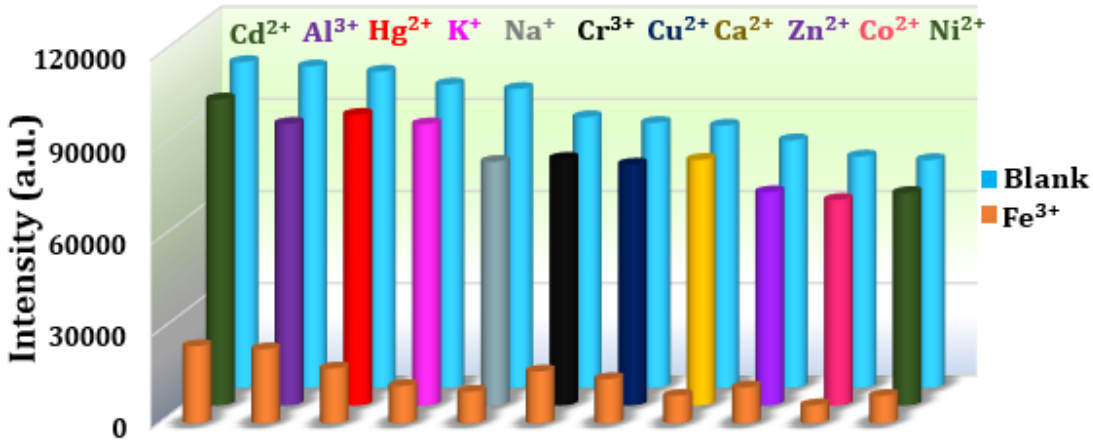

Figure S18: Bar diagram representation of Fe^{3+} quenching in presence of interfering ions.

Recyclability test for Fe^{3+} sensing:

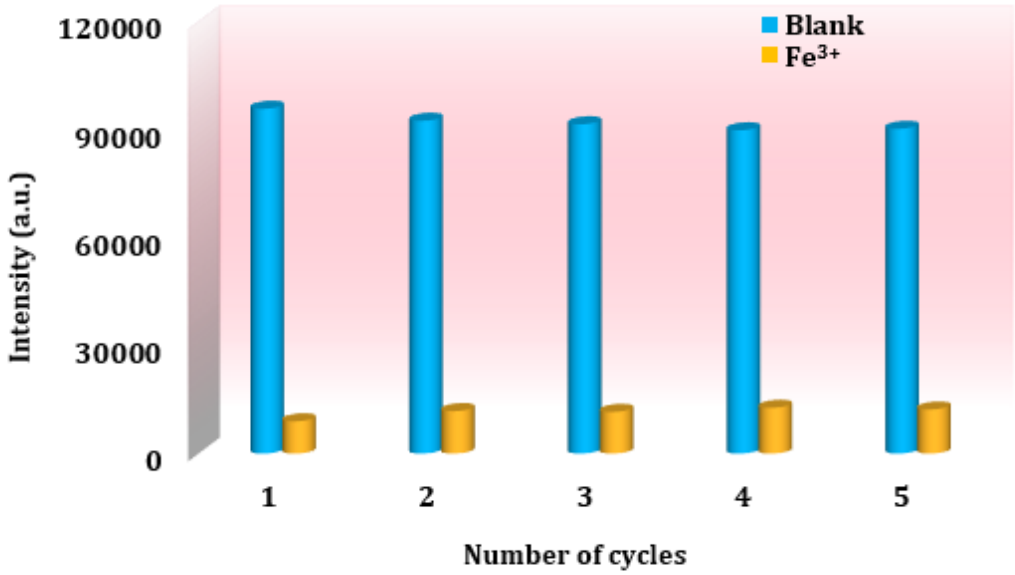

Figure S19: Recyclability of Fe^{3+} sensing using Zr-CPG xerogel.

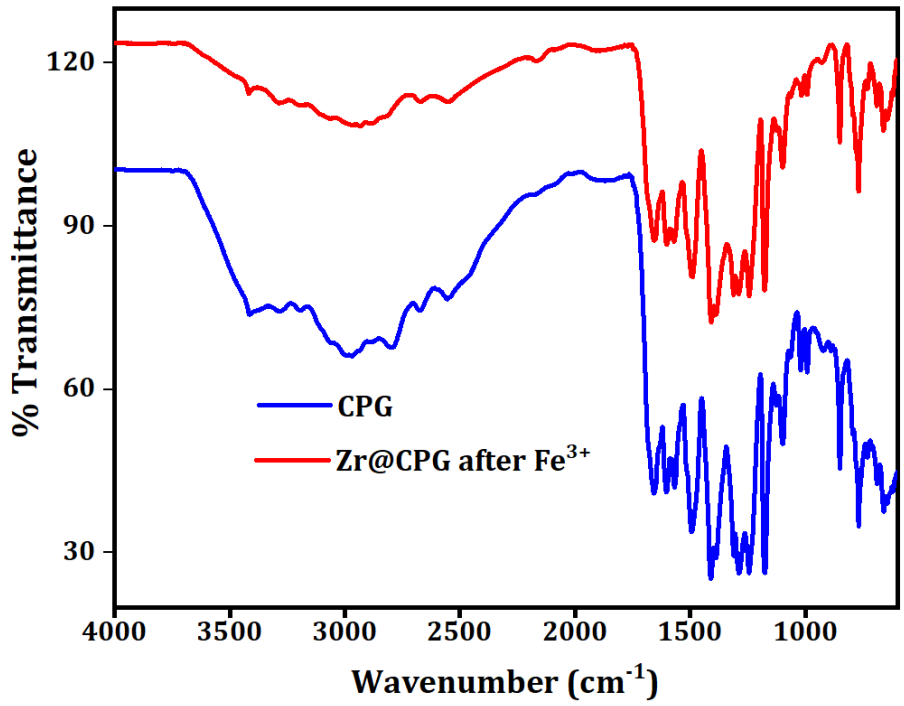

Figure S20: FT-IR spectra before and after completion of five cycles of NFT sensing.

Fe^{3+} sensing in physiological conditions:

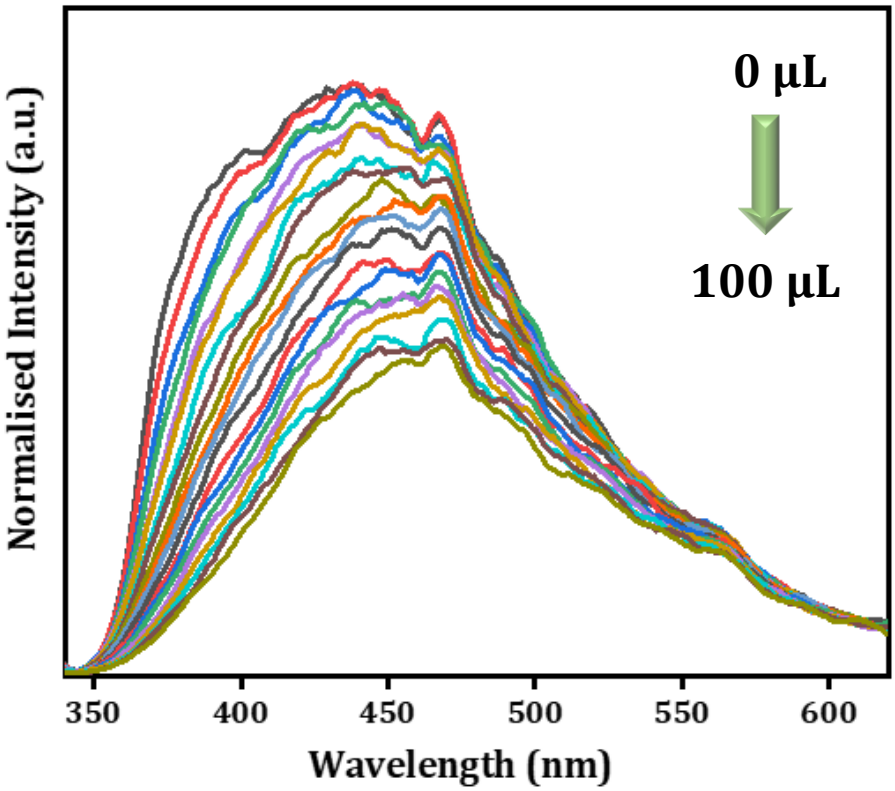

Figure S21: Quenching behaviour of Zr-CPG xerogel characteristic peak after adding 10 mM solution of NFT in physiological condition.

Quenching behaviour of Zr-CPG's characteristic luminescent peak upon addition of different antibiotics (Figure S22a-S22h):

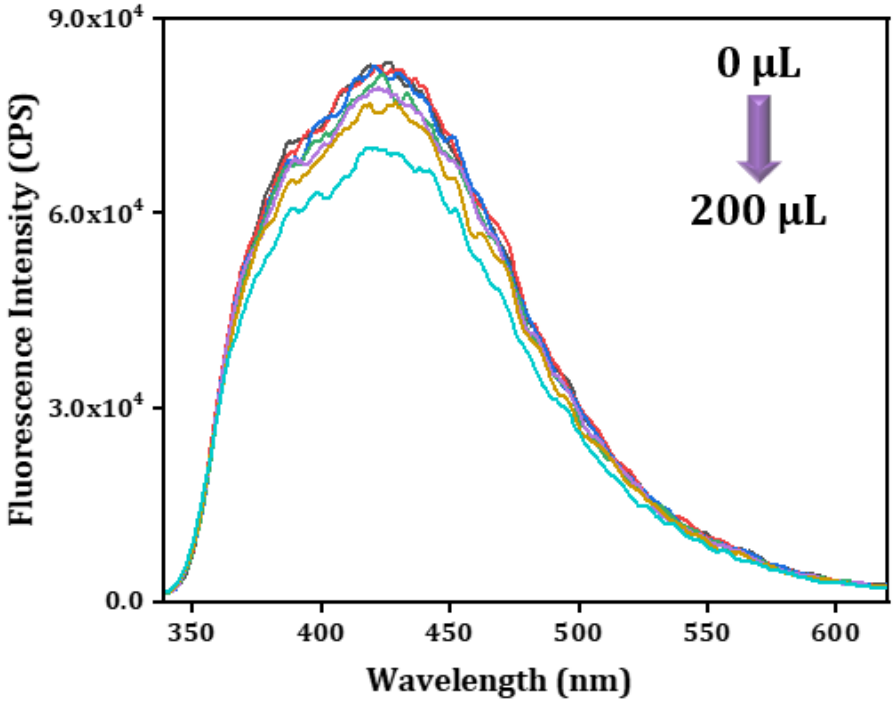

Figure S22a: Quenching of the luminescent peak of Zr-CPG xerogel upon addition of SDZ (10 mM, up to 200 µL).

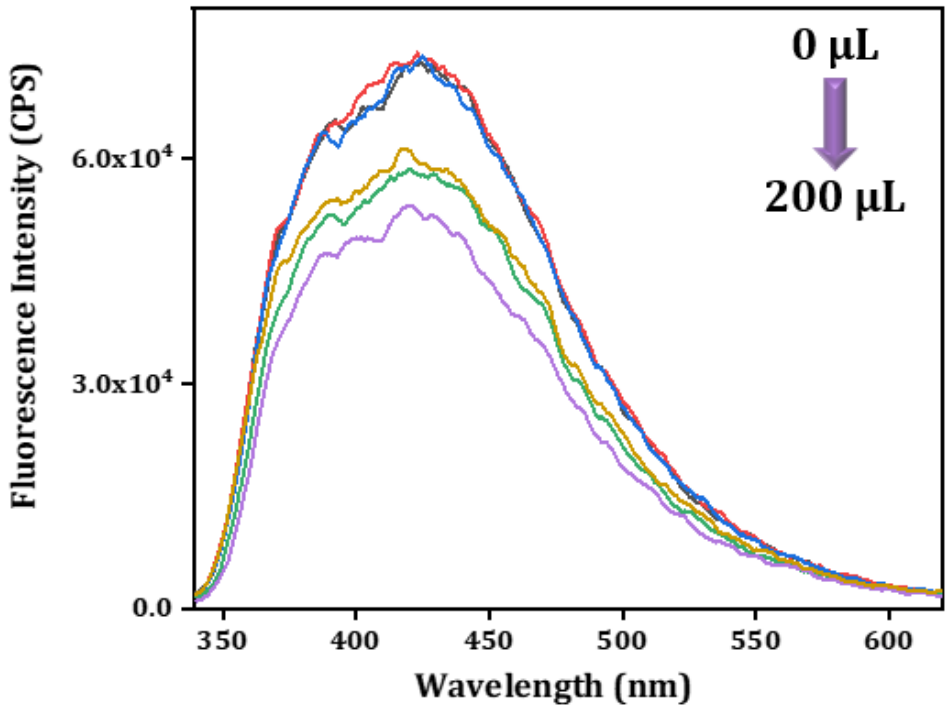

Figure S22b: Quenching of the luminescent peak of Zr-CPG xerogel upon addition of SMZ (10 mM, up to 200 µL).

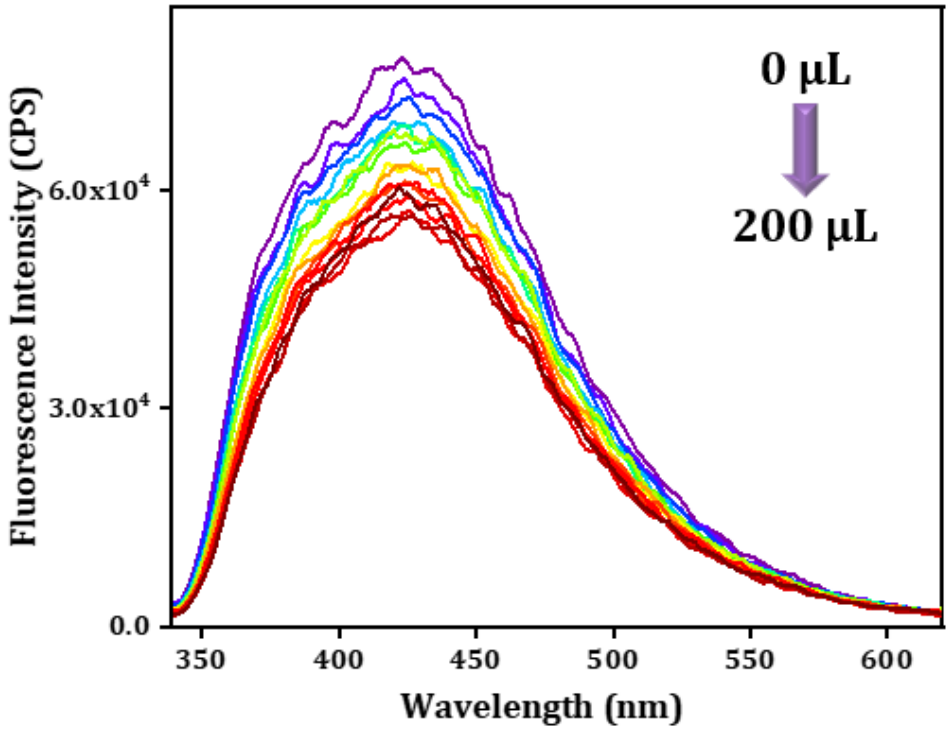

Figure S22c: Quenching of the luminescent peak of Zr-CPG xerogel upon addition of CAP (10 mM, up to 200 µL).

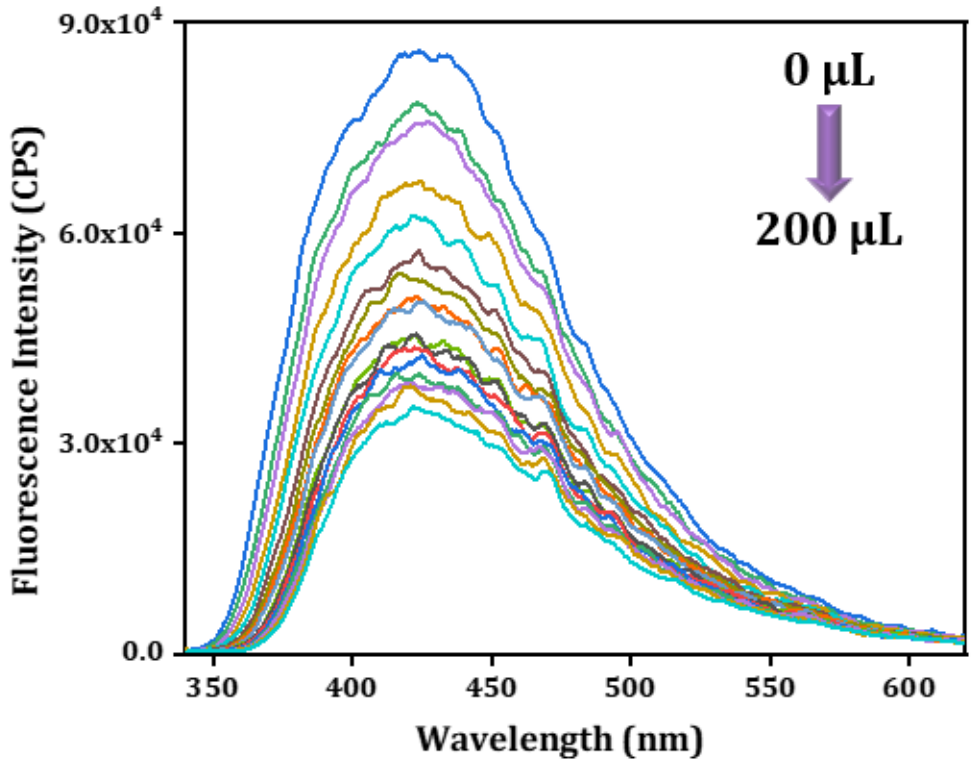

Figure S22d: Quenching of the luminescent peak of Zr-CPG xerogel upon addition of DTZ (10 mM, up to 200 µL).

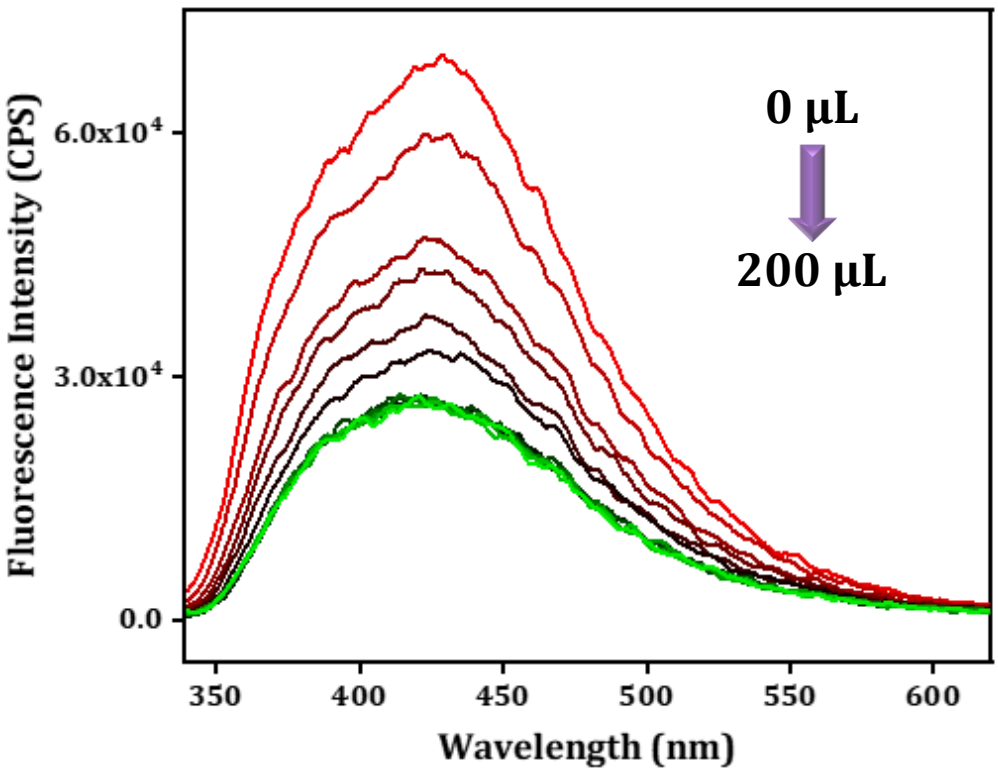

Figure S22e: Quenching of the luminescent peak of Zr-CPG xerogel upon addition of RDZ (10 mM, up to 200 µL).

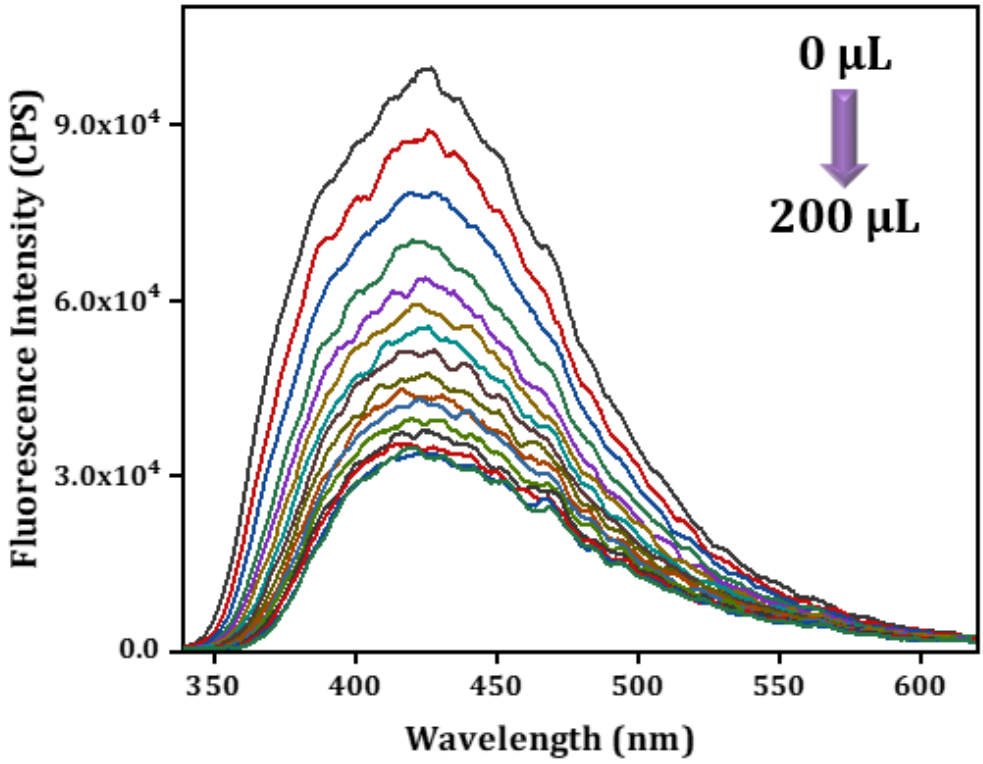

Figure S22f: Quenching of the luminescent peak of Zr-CPG xerogel upon addition of ODZ (10 mM, up to 200 µL).

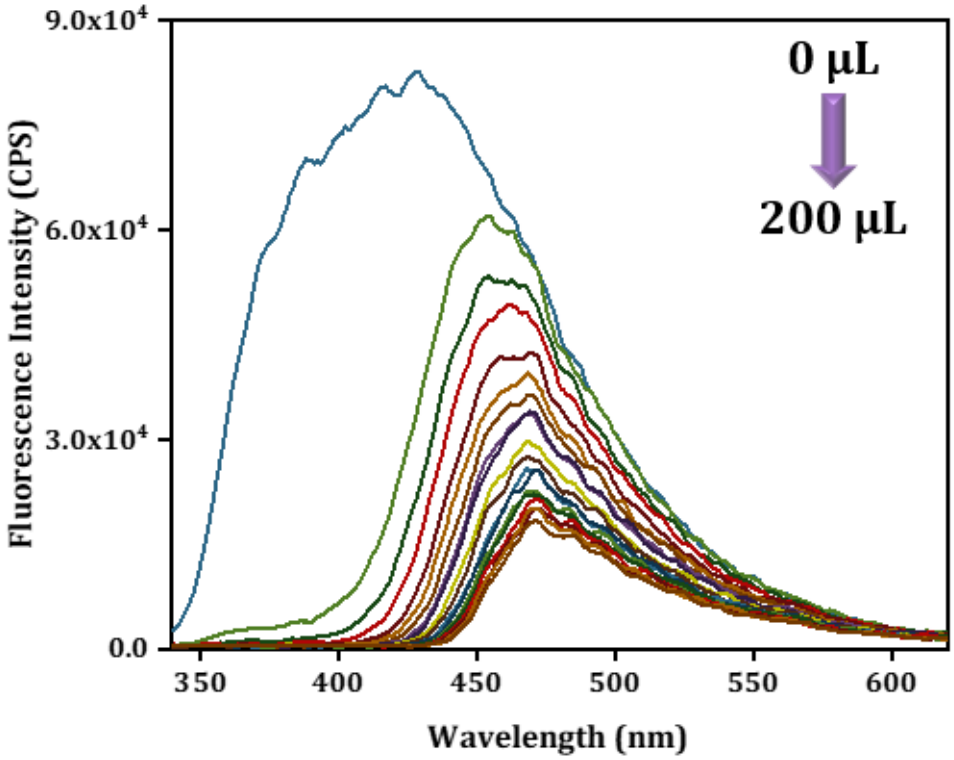

Figure S22g: Quenching of the luminescent peak of Zr-CPG xerogel upon addition of NFZ (10 mM, up to 200 µL).

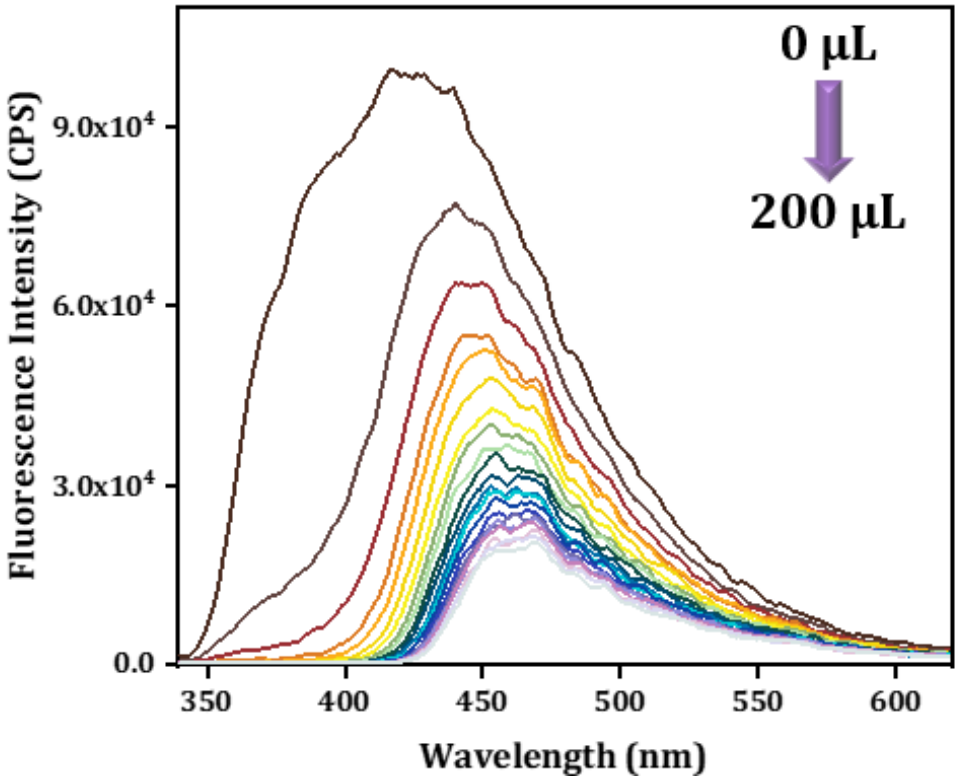

Figure S22h: Quenching of the luminescent peak of Zr-CPG xerogel upon addition of FZD (10 mM, up to 200 µL).

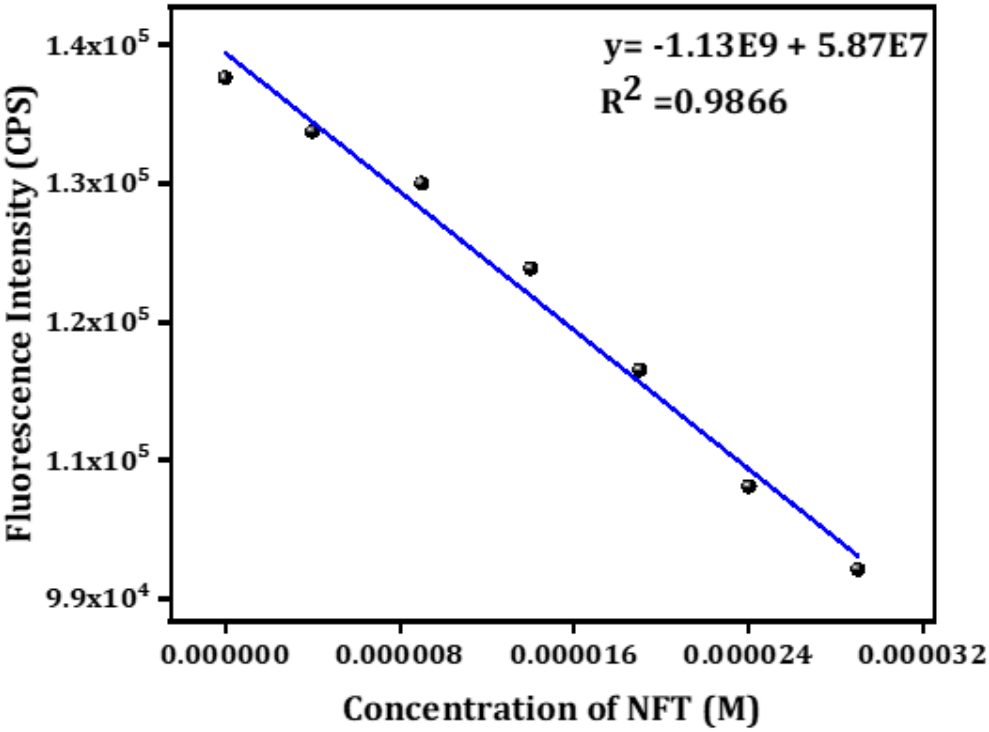

Figure S23: Fluorescence intensity changes of Zr-CPG xerogel with a function of NFT concentration.

NFT sensing in presence of interference antibiotics (Figure S24a-S24f):

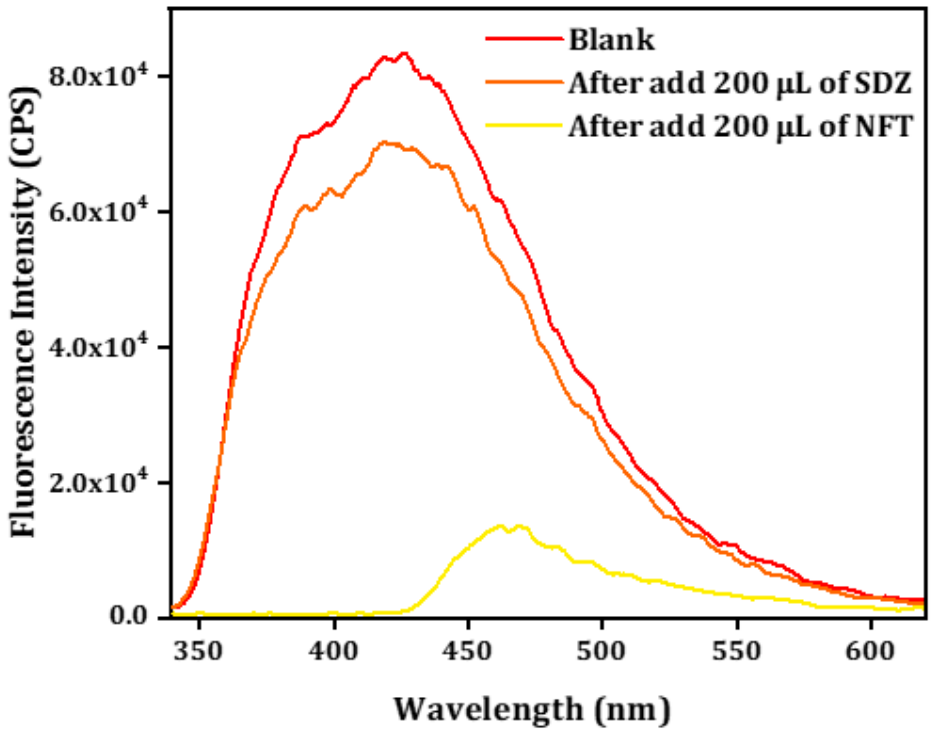

Figure S24a: Quenching behaviour of Zr-CPG xerogel characteristic peak after adding 10 mM solution of SDZ followed by NFT in water.

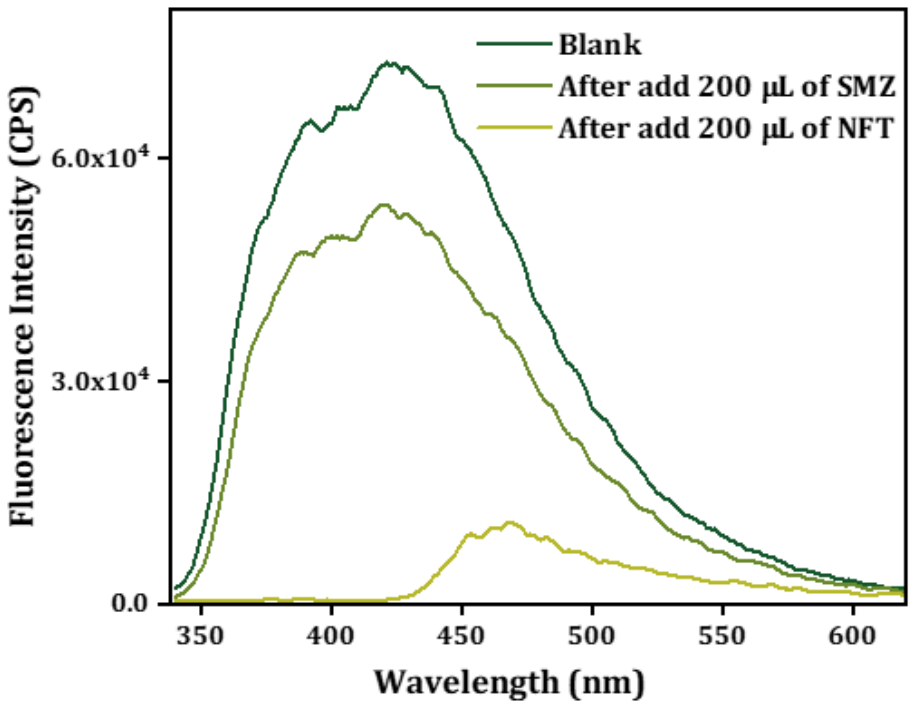

Figure S24b: Quenching behaviour of Zr-CPG xerogel characteristic peak after adding 10 mM solution of SMZ followed by NFT in water.

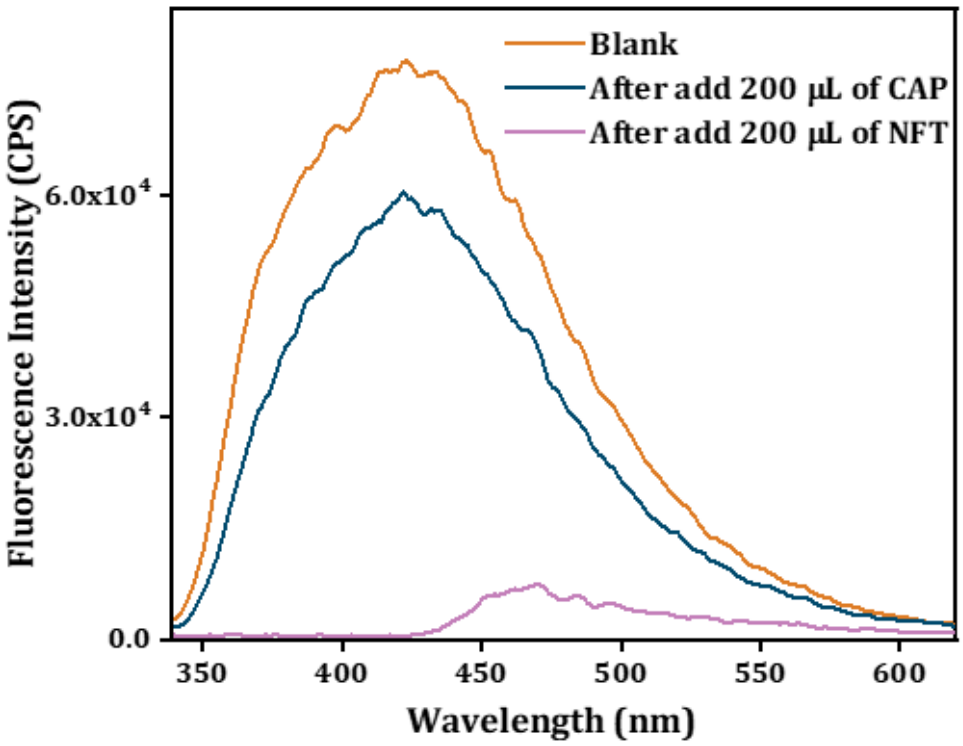

Figure S24c: Quenching behaviour of Zr-CPG xerogel characteristic peak after adding 10 mM solution of CAP followed by NFT in water.

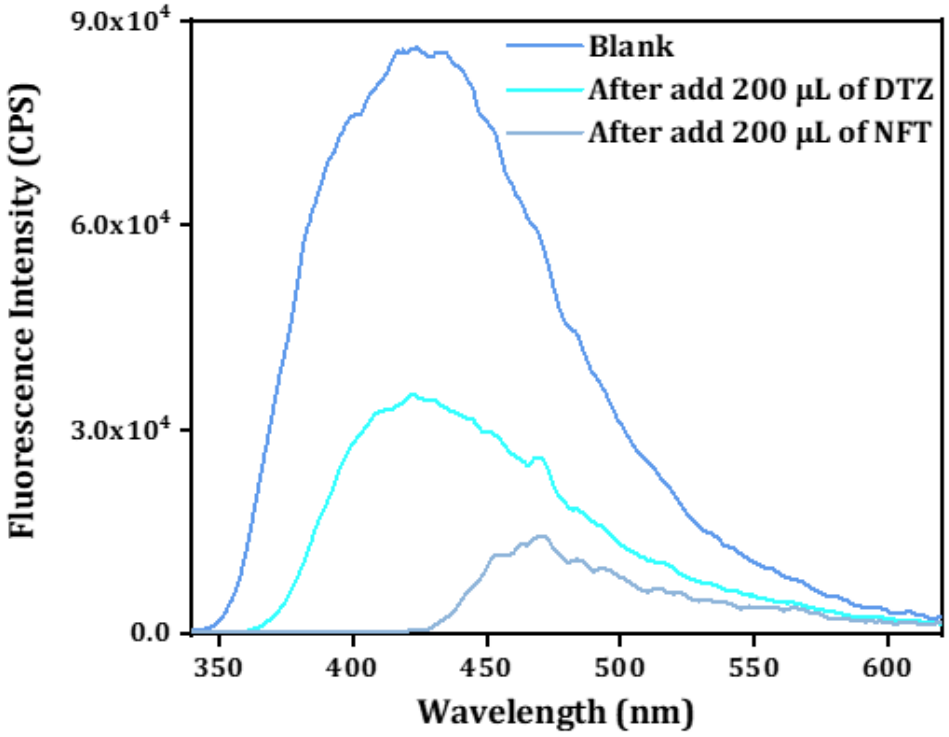

Figure S24d: Quenching behaviour of Zr-CPG xerogel characteristic peak after adding 10 mM solution of DTZ followed by NFT in water.

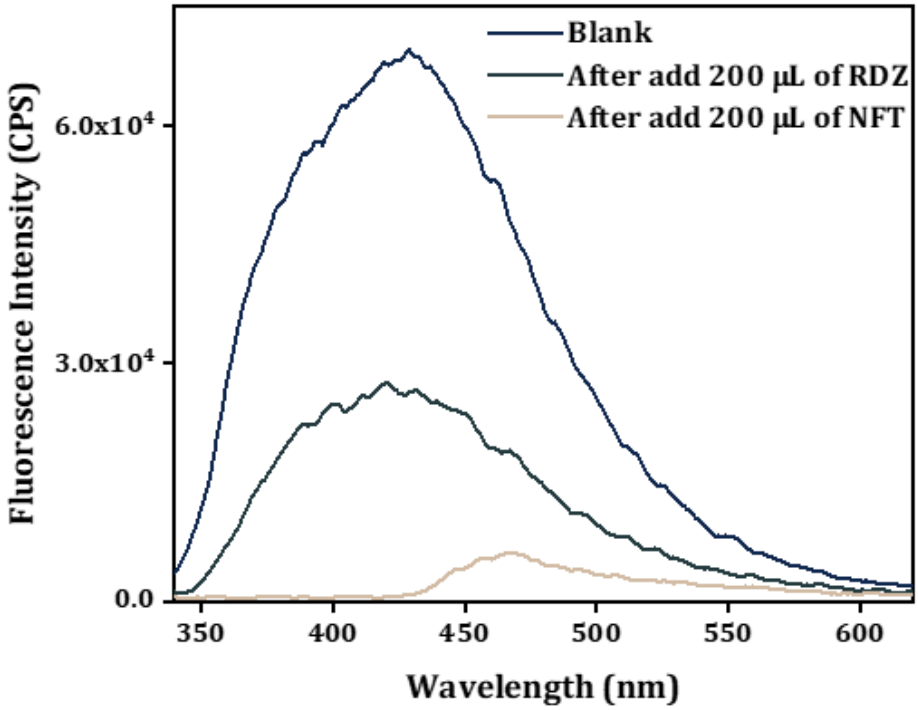

Figure S24e: Quenching behaviour of Zr-CPG xerogel characteristic peak after adding 10 mM solution of RDZ followed by NFT in water.

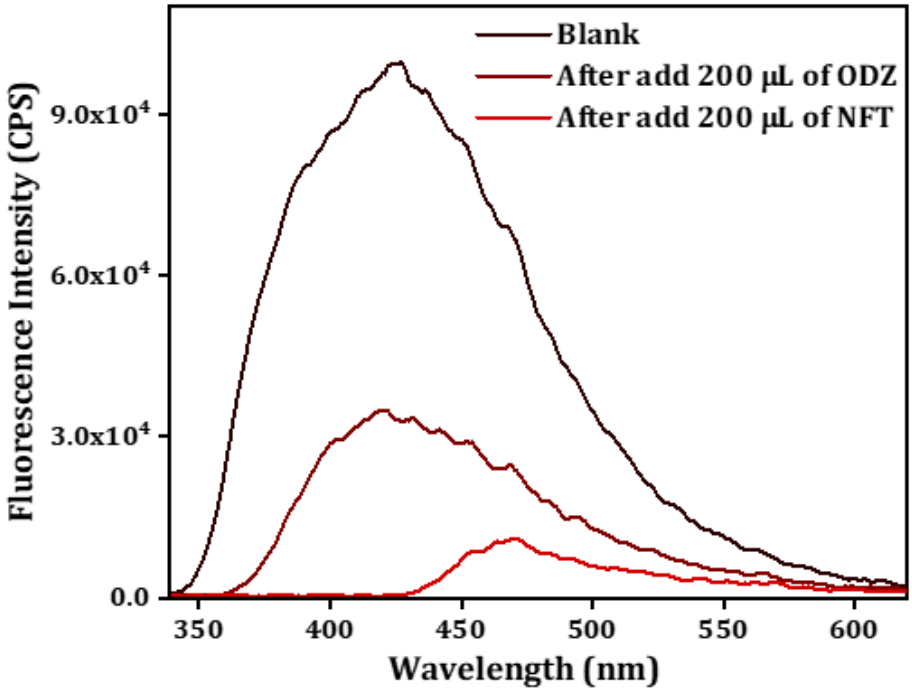

Figure S24f: Quenching behaviour of Zr-CPG xerogel characteristic peak after adding 10 mM solution of ODZ followed by NFT in water.

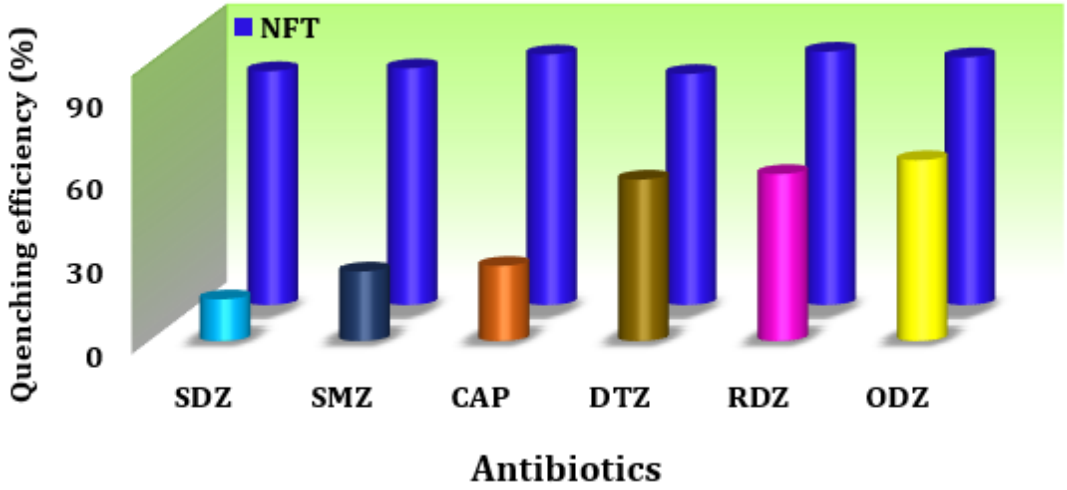

Figure S25: Quenching efficiency for NFT antibiotic in presence of other antibiotics (interference test).

Recyclability test for NFT sensing:

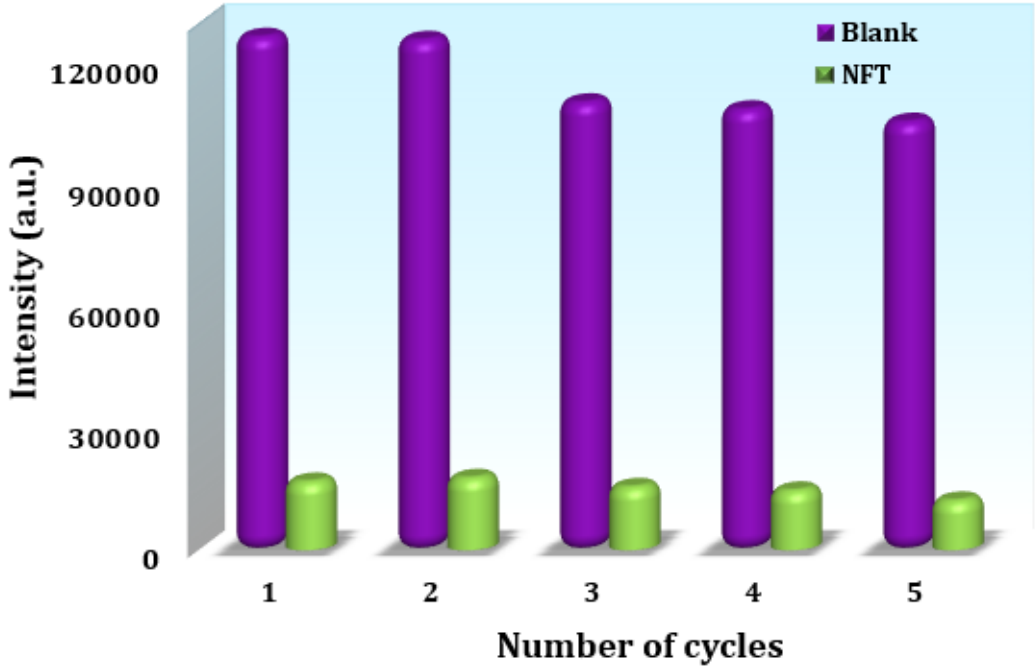

Figure S26: Recyclability of NFT sensing using Zr-CPG xerogel.

Fluorescence kinetic study for NFT sensing:

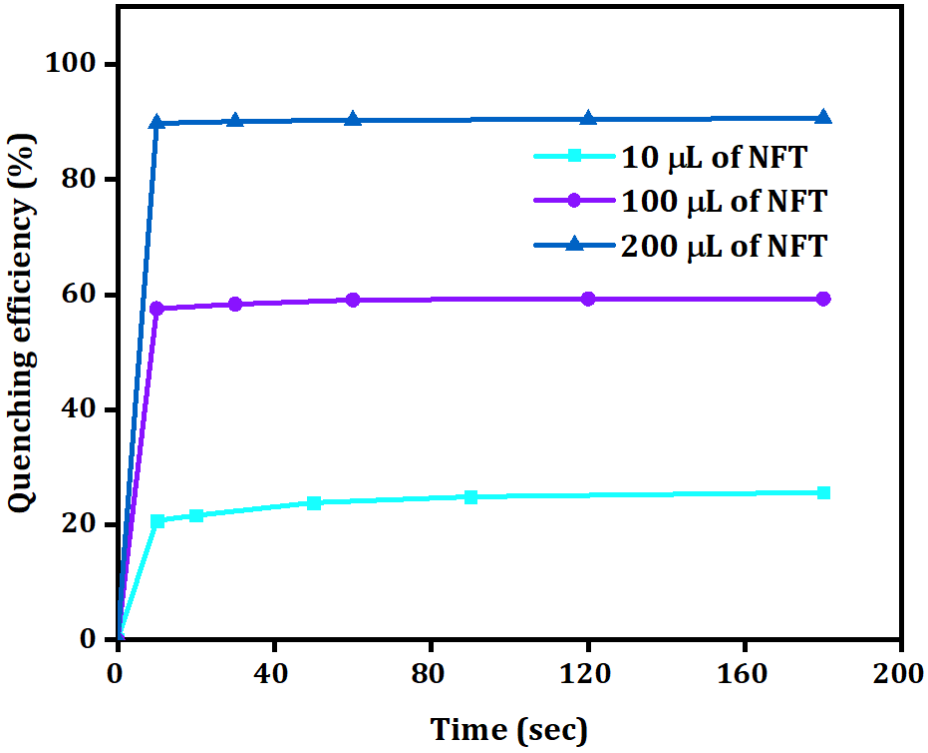

Figure S27: Kinetic study through fluorescence titration method for NFT sensing (variation in different volumes).

Comparison table of Fe^{3+} and NFT sensing for Zr-CPG xerogel with other reported materials:

Table S2: Comparison table for Fe^{3+} sensing of Zr-CPG xerogel with other reported materials.

Sl No.	Sensor probe	K_{SV} Value (M^{-1})	LOD value	Medium	Ref.
1.	Zr-CPG	7.16×10^3	68 ppb	Water	**This work**
2.	$[Zn_3(bpg)_{1.5}(azdc)_3]\cdot(DMF)_{5.9}\cdot(H_2O)_{1.05}$	2.54×10^4	1.71 ppm	DMF	1
3.	$[Tb(HL)(DMF)(H_2O)_2].3H_2O$	4.479×10^3	1.03 ppm	Water	2
4.	Al-MIL-53-N_3	6.13×10^3	0.03 μM	Water	3
5.	EuL_3	4.1×10^3	0.0005 mol/L	Water	4
6.	$[Zn_2(L1)_2(HBPT)_2]\cdot H_2O$	3.38×10^4	72 ppb	DMF	5
7.	Au NRs	-	100 ppb	Water	6
8.	AuNCs	-	3.5 μM	Water	7
9.	$[Cd(p\text{-CNPhHIDC})(4,4'\text{-bipy})_{0.5}]_n$	1.99×10^3	5×10^{-3} M	Water	8
10.	$[Zn(p\text{-CNPhHIDC})(4,4'\text{-bipy})]_n$	1.37×10^3	5×10^{-3} M	Water	
11.	BTP-1	-	0.74 nM	Water	9
12.	$[Zn_2(2,6\text{-NDC})_2(L).xG]_n$	-	0.052 ppm	DMF/ Water	10

Table S3: Comparison table for NFT sensing of Zr-CPG xerogel with other reported materials.

Sl No.	Sensor probe	K_{SV} Value (M^{-1})	LOD value	Medium	Ref.
1.	Zr-CPG	1.53×10^4	50 ppb	Water	**This work**
2.	Copper nanoclusters	4.3×10^3	0.73 μM	Phosphate buffer saline solution	11
3.	$Tb\text{-}(TATMA)(H_2O)\cdot2H_2O$	3.35×10^4	-	Water	12
4.	CTGU-8	9.25×10^5	52 ppb	Water	13
5.	Tb-AIP MMMs	4.0×10^4	0.30 μM	Water	14
6.	Eu-BCA thin-film	1.6×10^4	0.21 μM	Water	15
7.	$[Zn(IPT)_2]_n$	1.4×10^4	-	Water	16
8.	$[Cd(tptc)_{0.5}(bpy)]_n$	7.63×10^3	184 ppb	Water	17
9.	$Zn(L)(aip)\cdot(H_2O)$	-	100 ppm	Water	18
10.	$Zn(L)(ip)\cdot(DMF)(H_2O)_{1.5}$	-	80 ppm	Water	
11.	$Zn(L)(HBTC)\cdot(H_2O)_2$	-	45 ppm	Water	

Fluorescence quenching mechanism explanation:

Table S4: Average excited-state lifetime (<τ>) values of pristine Zr-CPG after the addition of 10 mM aqueous solution of Fe^{3+} ion and NFT.

	B_1 (%)	B_2 (%)	τ_1 (ns)	τ_2 (ns)	χ2	τ (ns)
Zr-CPG	45.89	54.11	0.69	2.76	1.04	2.40
Zr- CPG after adding Fe^{3+}	37.41	62.59	0.41	2.12	1.13	1.94
Zr-CPG after adding NFT	36.34	66.66	0.47	2.40	1.17	2.20

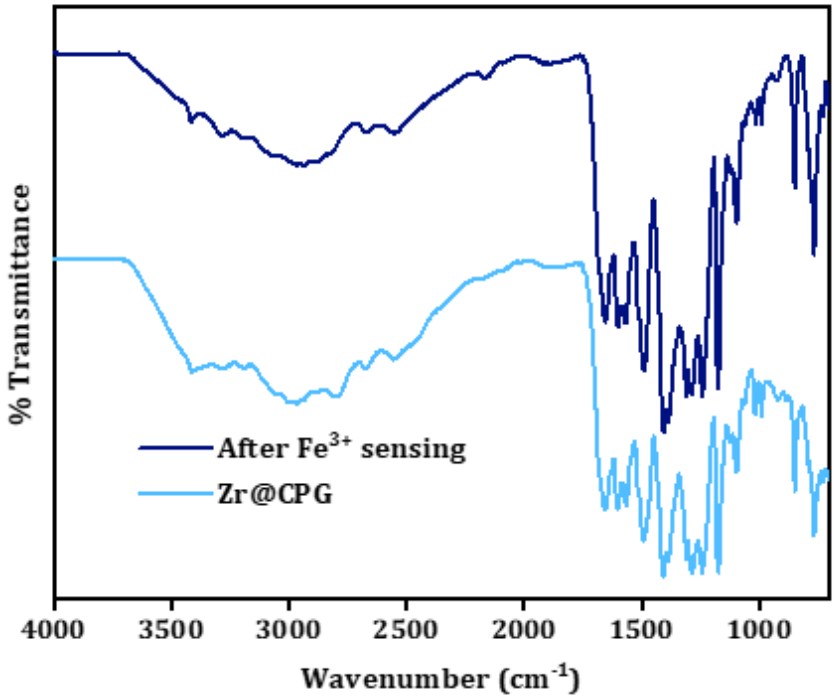

Figure S28: FT-IR spectra of Zr-CPG xerogel before and after Fe^{3+} sensing.

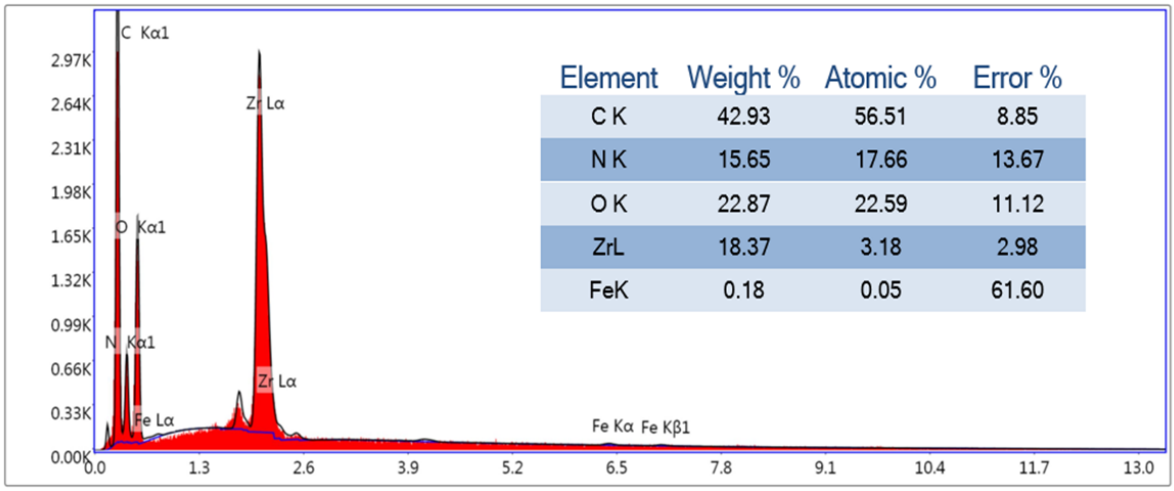

Element	Weight %	Atomic %	Error %
C K	42.93	56.51	8.85
N K	15.65	17.66	13.67
O K	22.87	22.59	11.12
ZrL	18.37	3.18	2.98
FeK	0.18	0.05	61.60

Figure S29: EDS analysis of Zr-CPG xerogel after NFT sensing.

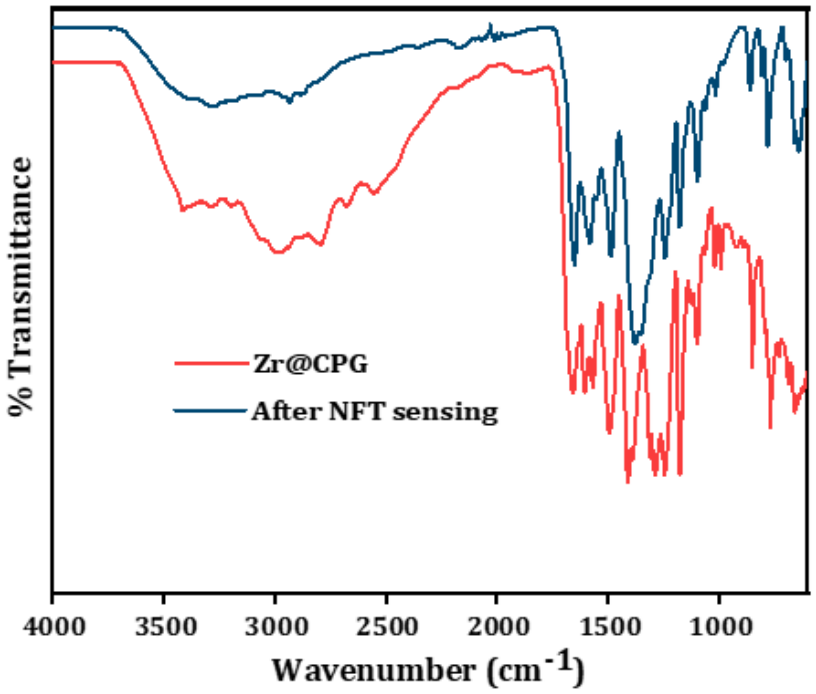

Figure S30: FT-IR spectra of Zr-CPG xerogel before and after NFT sensing.

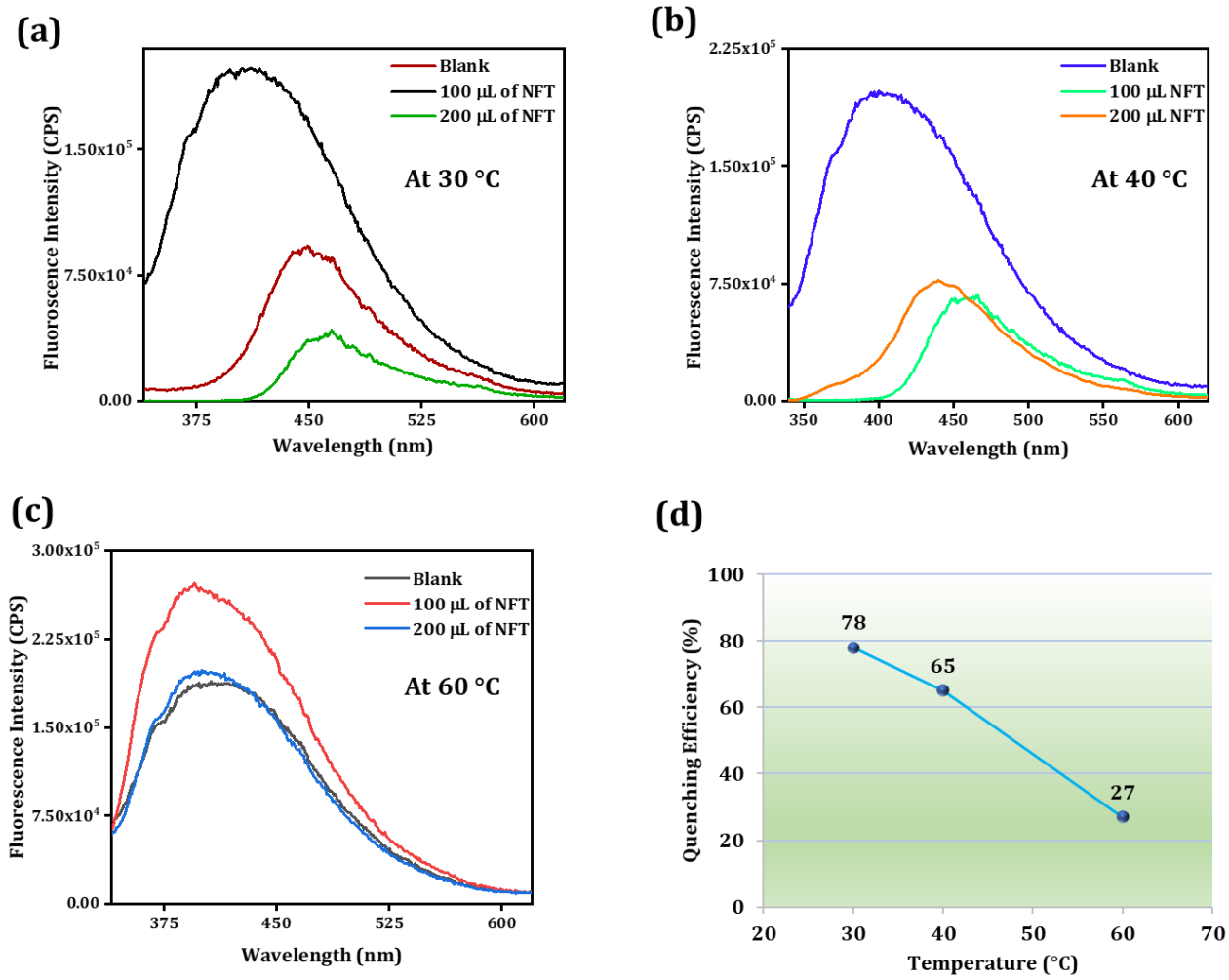

Figure S31: Temperature dependent quenching study (a-c), (d) corresponding line graph to dictate quenching efficiency.

Optimized structure of linker and all antibiotics

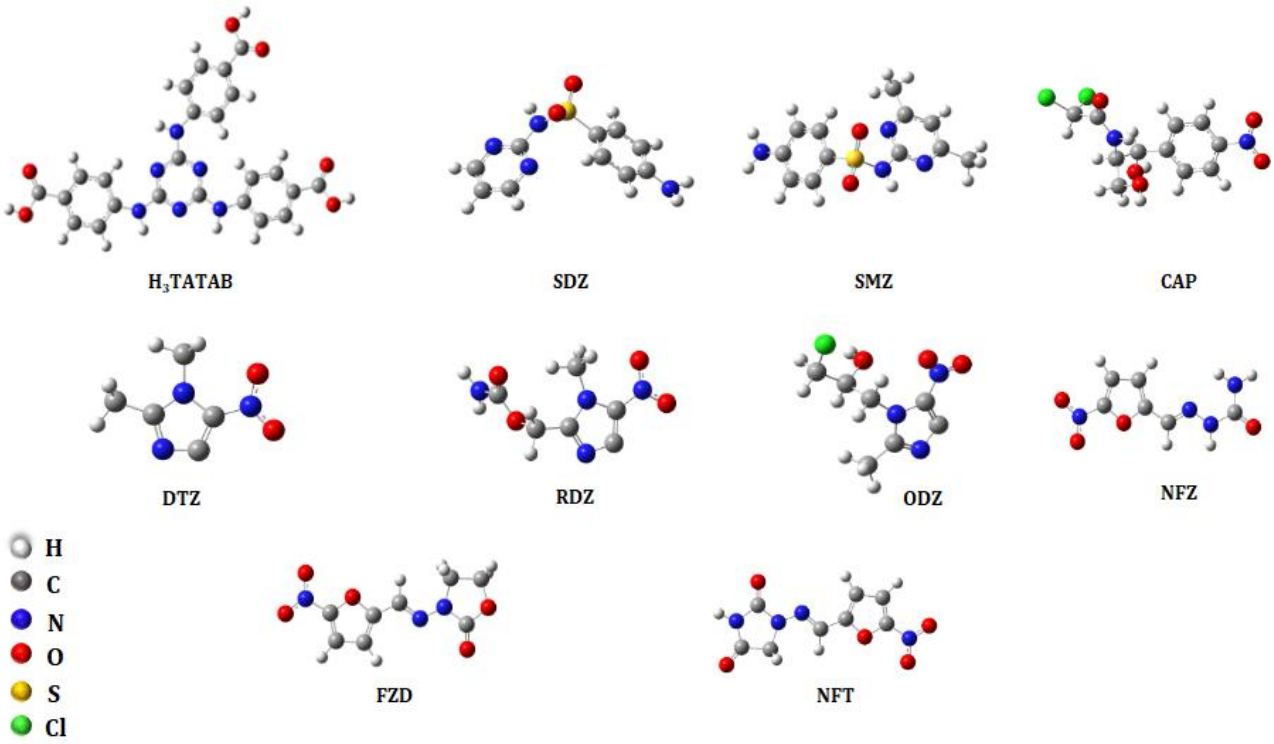

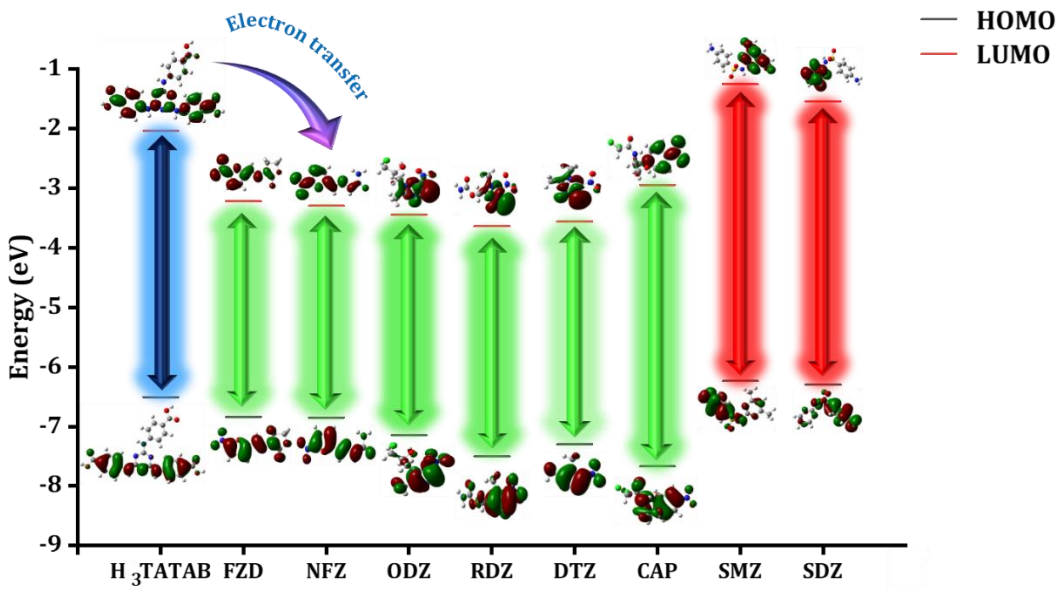

Figure S32: HOMO-LUMO energy levels of the linker (H_3TATAB) and all antibiotics (except NFT).

Table S5: HOMO-LUMO energy levels of the linker (H_3TATAB) and all antibiotics with calculated band gaps.

Compound	HUMO (eV)	LUMO (eV)	Band Gap (eV)
H_3TATAB	-6.51	-2.04	4.47
NFT	-6.99	-3.34	3.65
FZD	-6.84	-3.22	3.62
NFZ	-6.85	-3.30	3.55
ODZ	-7.14	-3.45	3.69
RDZ	-7.50	-3.64	3.86
DTZ	-7.30	-3.56	3.74
CAP	-7.67	-2.95	4.72
SMZ	-6.24	-1.26	4.98
SDZ	-6.30	-1.55	4.75

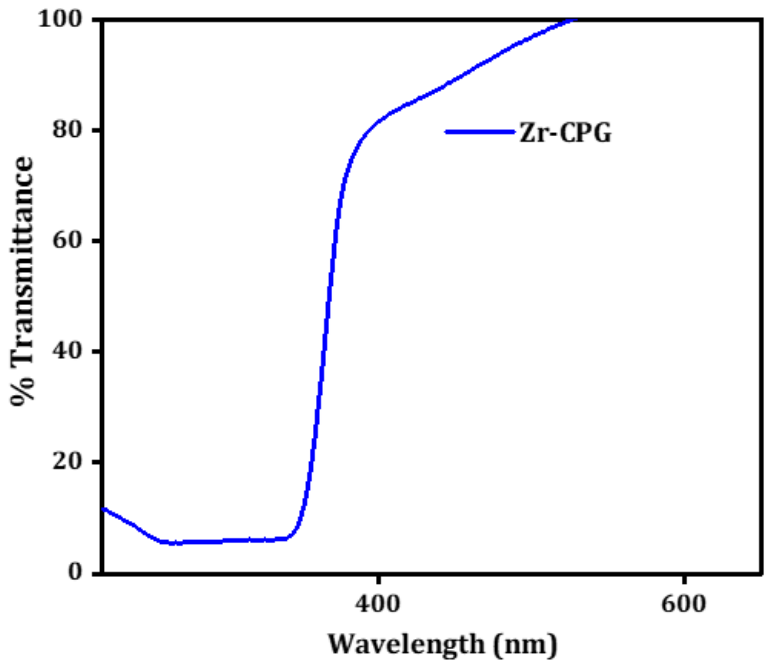

Figure S33: DRS spectra of Zr-CPG.

Reference:

1. R. Goswami, S. C. Mandal, B. Pathak and S. Neogi, *ACS Appl. Mater. Interfaces*, 2019, **11**, 9042-9053.
2. S.-T. Zhang, J. Yang, H. Wu, Y.-Y. Liu and J.-F. Ma, *Chem. Eur. J.*, 2015, **21**, 15806-15819.
3. A. Das, S. Banesh, V. Trivedi and S. Biswas, *Dalton Trans.*, 2018, **47**, 2690-2700.
4. M. Zheng, H. Tan, Z. Xie, L. Zhang, X. Jing and Z. Sun, *ACS Appl. Mater. Interfaces*, 2013, **5**, 1078-1083.
5. Z.-Q. Liu, K. Chen, Y. Zhao, Y.-S. Kang, X.-H. Liu, Q.-Y. Lu, M. Azam, S. I. Al-Resayes and W.-Y. Sun, *Cryst. Growth Des.*, 2018, **18**, 1136-1146.
6. S. Thatai, P. Khurana, S. Prasad and D. Kumar, *Microchem. J.*, 2014, **113**, 77-82.
7. J.-a. Annie Ho, H.-C. Chang and W.-T. Su, *Anal. Chem.*, 2012, **84**, 3246-3253.
8. J. Zhang, L. Zhao, Y. Liu, M. Li, G. Li and X. Meng, *New J. Chem.*, 2018, **42**, 6839-6847.
9. J. Nandre, S. Patil, V. Patil, F. Yu, L. Chen, S. Sahoo, T. Prior, C. Redshaw, P. Mahulikar and U. Patil, *Biosens. Bioelectron.*, 2014, **61**, 612-617.
10. D. Mukherjee, A. Pal, S. C. Pal, A. Saha and M. C. Das, *Inorg. Chem.*, 2022, **61**, 16952-16962.
11. Z. Cai, S. Pang, L. Wu, E. Hao and J. Rong, *Spectrochim. Acta A Mol. Biomol. Spectrosc.*, 2021, **255**, 119737.
12. Q.-Q. Zhu, H. He, Y. Yan, J. Yuan, D.-Q. Lu, D.-Y. Zhang, F. Sun and G. Zhu, *Inorg. Chem.*, 2019, **58**, 7746-7753.
13. Z.-H. Zhou, W.-W. Dong, Y.-P. Wu, J. Zhao, D.-S. Li, T. Wu and X.-h. Bu, *Inorg. Chem.*, 2018, **57**, 3833-3839.
14. F. Zhang, H. Yao, Y. Zhao, X. Li, G. Zhang and Y. Yang, *Talanta*, 2017, **174**, 660-666.
15. F. Zhang, H. Yao, T. Chu, G. Zhang, Y. Wang and Y. Yang, *Chem. Eur. J.*, 2017, **23**, 10293-10300.
16. M. Liu and Y. Chi, *J. Fluoresc.*, 2020, **30**, 1035-1042.
17. L. Fan, F. Wang, D. Zhao, X. Sun, H. Chen, H. Wang and X. Zhang, *Spectrochim. Acta A Mol. Biomol. Spectrosc.* 2020, **239**, 118467.
18. Z. Zhou, M.-L. Han, H.-R. Fu, L.-F. Ma, F. Luo and D.-S. Li, *Dalton Trans.*, 2018, **47**, 5359-5365.